express the measured intensity as

$$I_\nu = I_{o,\nu}\mathcal{R}_\nu \exp\left[-\tau_\nu(0,p_s)\left(\frac{1}{\mu_o}+\frac{1}{\mu_s}\right)\right] \tag{3.40}$$

where μ_o and μ_s are cosines of the sun's zenith angle, θ_o, and the satellite's view angle, θ_s, respectively. $\mathcal{R}_\nu$ is the ocean reflection function (this is a bidirectional reflection function as described in Chapter 4), $I_{o,\nu}$ is the inflowing solar radiation at the top of the atmosphere, and $\tau_\nu(0,p_s)$ is the optical depth associated with oxygen A band absorption along the vertical path from the satellite to the ocean surface. This optical depth may be expressed as a function of surface pressure p_s according to

$$\tau_\nu(0,p_s) = \frac{r}{g}\int_0^{p_s} k_{\nu,m}(p)\,dp = t(p_s) \tag{3.41}$$

where $t(p_s)$ is left as an unspecified function of surface pressure (an example of this function is a subject of Problem 3.7). We recognize that the effects of pressure broadening complicate this integration and neglect the effects of temperature on absorption. Thus a ratio of two measurements at frequencies ν_1 and ν_2 in the A band provides

$$\frac{I_{\nu_1}}{I_{\nu_2}} = \frac{I_{o,\nu_1}}{I_{o,\nu_2}}\frac{\mathcal{R}_{\nu_1}}{\mathcal{R}_{\nu_2}} \exp\left[-\Delta\tau_\nu(0,p_s)\left(\frac{1}{\mu_o}+\frac{1}{\mu_s}\right)\right] \tag{3.42}$$

where $\Delta\tau(0,p_s) = \tau_{\nu_1} - \tau_{\nu_2}$. If the frequencies ν_1 and ν_2 are close enough, then $\mathcal{R}_{\nu_1} \approx \mathcal{R}_{\nu_2}$ and assuming that I_{o,ν_1} and I_{o,ν_2} are also known, as is the viewing angle of the satellite ($\mu_s = \cos\theta_s$) and the solar elevation, then $\Delta\tau_\nu(0,p_s)$ can be retrieved by a simple inversion of (3.42). The surface pressure then follows from (3.41) provided the absorption coefficients at ν_1 and ν_2 are sufficiently well known and the function $t(p_s)$ is invertible.

This approach is essentially that proposed by Barton and Scott (1986) who recommended choosing ν_1 and ν_2 to coincide with the center frequencies of the P and R branches of the A band. However, a more detailed analysis of Mitchell and O'Brien (1987) demonstrated that this approach is only able to produce surface pressure estimates to 2 mb which is considered marginally acceptable for weather prediction requirements. One of the basic problems that arises is the temperature dependence of the absorption on the P and R branches (as discussed previously in relation to Fig. 3.14), which introduces further complications in (3.41). A second problem is the lack of discrimination between atmospheric reflections from aerosol and molecules and the reflection from the surface. Since photons reflected back to the satellite from the atmosphere do not flow through the full depth of the atmosphere, they represent a source of error in retrieving p_s. The magnitude of this error is variable, depending on the aerosol loading. Mitchell and O'Brien have proposed that observations at multiple wavelengths throughout the A band at a 1 cm^{-1} resolution might overcome these problems.

3.6 Passive Spectrometer Systems

Measurement of the Earth's radiation at a spectral resolution high enough to study details of molecular absorption bands is achieved using spectrometer sensor systems. Three major classifications of optical spectrometer systems will now be discussed. There are also various categories of microwave systems and some reference to these is given in the notes at the end of this chapter.

Optical spectrometers can be considered in terms of prism dispersion, grating diffraction, and radiation interference. Examples of each of these will now be described.

3.6.1 Prism Spectrometers

The first step in analyzing light was made by Newton in 1666 when he developed an early form of the prism spectrometer. In a prism spectrometer, the property of *dispersion* is employed to separate the various wavelengths of the light as it enters the system. Figure 3.21 shows an idealized and highly simplified laboratory arrangement of a prism spectrometer. Light from a source is made parallel by the lens L. When this parallel beam passes through a prism, rays of different wavelengths are dispersed (bent) to varying degrees depending on the refractive index of the prism (much more is said about refractive index in Chapter 4). Thus, radiation at different wavelengths is projected at different positions on the screen after being focused by a second lens L'. To each wavelength a line that is the image of the slit appears on the screen. Radiation of a particular wavelength can be then detected either by turning the prism slightly so that light of a different wavelength falls on a detector fixed at some location on the screen or by holding a prism fixed and moving the detector along the screen.

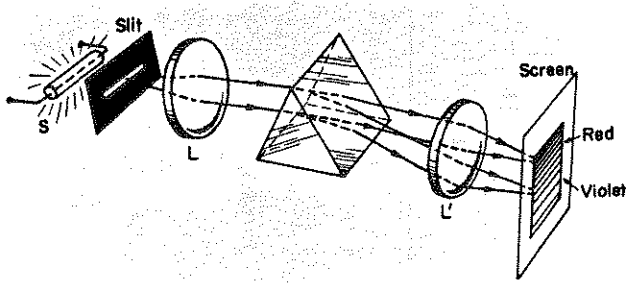

Figure 3.21 The principle of the prism spectrometer. This particular design was introduced by Joseph Fraunhofer in the nineteenth century and provided a way of sharply separating the colors of light.

Prism spectrometers are typically used in imaging devices. The spectral resolution achieved with a prism spectrometer depends on the optical layout of the instrument and the size of the prism. Typical resolutions, however, are an order of magnitude less than that of a grating spectrometer.

Prism spectrometers, despite their coarse resolution, provide important information about the atmosphere. The Dobson spectrometer is perhaps the best known example of this type of spectrometer. Dobson (1957) provides a detailed description of the spectrometer and how to operate it. A simplified layout of the spectrometer optics is shown in Fig. 3.22. Light enters a window W at the top of the instrument and, after reflection by a right–angled prism, falls on a slit S_1 of a spectroscope. The spectroscope consists of a quartz collimating lens from which the light enters a 60 % prism. A mirror then reflects the light back through the same prism and lens to form a spectrum in the focal plane of the instrument. This double–pass configuration improves the spectral resolution of the spectrometer. The required wavelengths are isolated by means of slits (S_2, S_3, and S_4) in the focal plane. In the actual instrument, the light is passed through a second spectroscope (not shown) so that the shorter wavelength ultraviolet can be separated further from longer UV wavelengths before being detected. The thick flat quartz plate (Q_1) located in front of slit S_1 is used as a fine scale wavelength adjustment. When the plates are inclined to the direction of the ray of light, the ray is

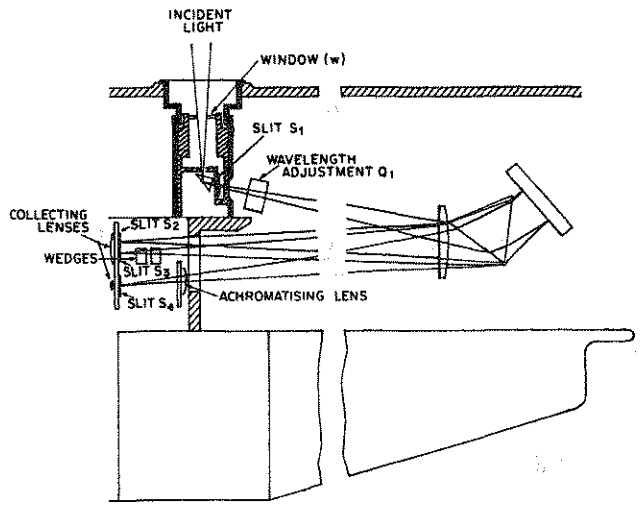

Figure 3.22 The optical layout of a Dobson spectrometer simplified.

refracted and displaced upward or downward. By this means, the wavelength of the radiation falling on the detector (a photomultipler) can be changed by accurately known amounts. The wavelength of the ray passing slit S_2 can be made of any value between about 0.305μm and 0.352μm. Slight adjustments to the instrument are needed to take account of air temperature changes, which slightly alter the refractive index of the quartz plate. The actual theory of ozone retrieval based on these measurements is discussed in more detail in Chapter 6.

3.6.2 Grating Spectrometers

The development of the diffraction grating by Fraunhofer in the nineteenth century provided a new tool for analyzing radiation that far exceeded prisms in its ability to disperse light. The working of a diffraction grating can be understood in the context of a wave flowing through a single long rectangular slit. According to Huygens' principle, when the incident wave falls on the slit all points along the wave front become secondary sources of waves producing new

waves called *diffracted* waves. Observing the diffracted wave at different angles θ with respect to the direction of incidence, we find a distinct pattern of light appearing (the *diffraction pattern*) where the intensity is zero in certain directions. These zero–intensity points are referred to as null points, and their position is defined in the following way. Suppose the distance CD in Fig. 3.23a is one–half a wavelength, then the wave from A is exactly out of phase with the wave from C. In fact every ray from the first half of the slit (AC) is exactly canceled by a ray from CB, originating at a point $b/2$ away where b is the width of the slit. This condition may be stated as

$$\frac{b}{2}\sin\theta = \frac{n}{2}\lambda \tag{3.43}$$

where n is an integer, b is the width of the slit, and λ is the wavelength of the incident wave. According to this formula, the null points for radiation of different wavelengths occur at different values of θ.

Consider the diffraction pattern produced by a large number of parallel narrow slits of equal width and equal spacing (Fig. 3.23b). The pattern consists of a series of maxima and minima associated with the interference of the light from one slit to another. The location of the maxima of the interference pattern is given by

$$a\sin\theta = m\lambda \tag{3.44}$$

where $m = 0, \pm1, \pm2, \ldots$ Superimposed on these interference maxima is the diffraction pattern of the single slit. According to the value of m in (3.44), the principal maxima are referred to as first, second, third and so on, order of diffraction.

A system such as the one just described is called a *transmission diffraction grating*. For the purposes of analyzing infrared, visible, or ultraviolet light, transmission diffraction gratings consist of several thousands of slits per centimeter, obtained by etching a series of parallel lines on transparent film. A diffraction grating can also work by reflection in which case the grating consists of a series of parallel lines that are etched on a metallic surface. Transmission gratings generally perform poorly in comparison with reflection gratings, which are used in high performance space spectrometers.

A simple arrangement for a grating spectrometer is shown in Fig. 3.24a. When light of several wavelengths falls on the grating, diffraction orders (maxima) at different angles, prescribed by (3.44),

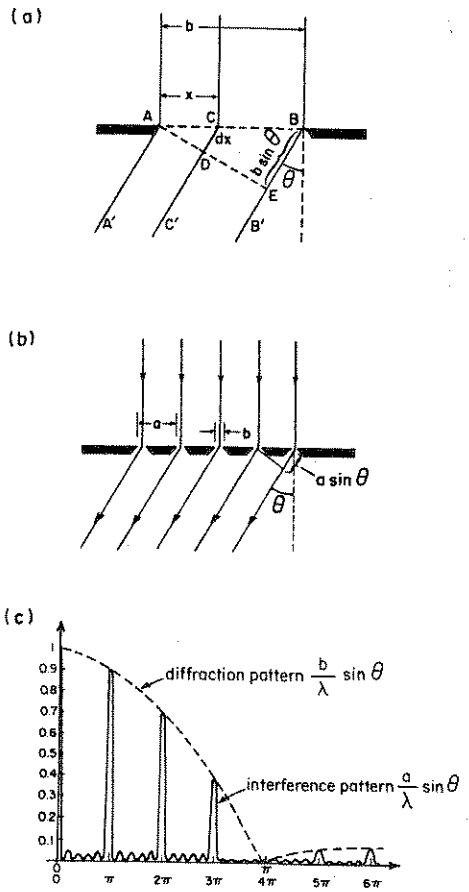

Figure 3.23 (a) The simple geometry of diffraction by a single slit and the diffraction geometry for multiple slits. (b) The cross section of a (transmission) diffraction grating. (c) The diffraction pattern from an eight slit grating. The lower abscissa is the value of θ in (3.44) corresponding to the various diffractions orders.

are produced. Each diffraction order displays the spectrum of the source. Note that the longer the wavelength, the more the radiation is deviated for a given order of the spectrum. An important point here is that the diffraction curve associated with a particular higher order n_2 of a shorter wavelength λ_2 overlaps the patterns of another longer wavelength λ_1 of order n_1 when $n_1\lambda_1 = n_2\lambda_2$. That is, first–order red light at 0.7 μm is overlapped by second–order blue light of wavelength 0.35 μm. If we are interested in sensing red light, then the low–order shortwave light must be removed which is usually achieved by a blocking filter.

The grating spectrometer has been widely used in remote sensing. The satellite infrared spectrometer (SIRS), launched in April 1989 on NIMBUS 3, was the first space–based grating spectrometer used for vertical temperature sounding experiments. Several other grating systems are now flown. One specific example is the solar backscatter ultraviolet (SBUV) instrument used for the total ozone mapping which monitors UV radiation in a number of selected wavelength bands. Another grating system is the coastal zone color scanner (CZCS) flown on the NIMBUS 7 satellite which is devoted to the study of ocean color in an effort to discriminate between organic and inorganic materials in water. A third example is the stratospheric aerosol and gas experiment (SAGE) sensor. The optical layout of the SAGE I sensor is shown in detail in Fig. 3.24b. The sensor is designed to monitor solar radiation in four bands centered at 0.385μm, 0.45μm, 0.6μm, and 1.0μm in an effort to obtain profiles of stratospheric aerosol, ozone, and nitrogen dioxide. The optical module consists of a flat scanning mirror that directs the solar radiation into the system, a telescope which directs the radiation to the grating, and four silicon detectors positioned to measure the radiation reflected from the grating at the wavelength selected. Each detector is filtered to remove contributions from unwanted grating orders.

3.6.3 Interferometer Spectrometers

The third type of optical system works quite differently from a prism or a grating and is based on the optical instrument invented by A. A. Michelson in 1880 named the *interferometer*. The role of the prism and grating in the previous systems is to separate the different spectral elements into different directions so they can be individually measured. The interferometer makes no use of dispersion of light; rather, it makes use of interference effects. In Michelson's interferom-

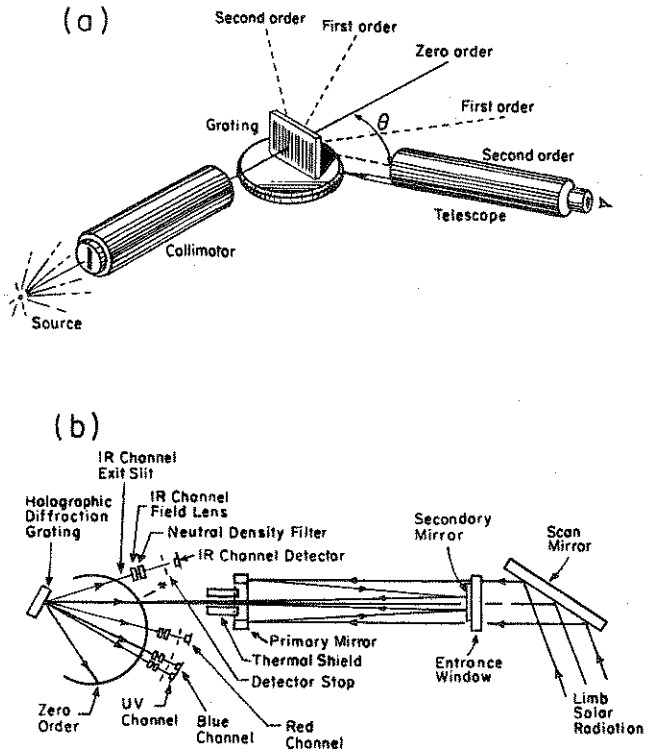

Figure 3.24 (a) A grating spectrometer. In the setup shown, light is collimated and flows onto a transmission grating. The spectra of different orders are measured by moving the detector. (b) A schematic of the SAGE I optical system including fixed, multiple detectors (channels).

eter light split into two beams by a half–reflecting glass plate follows two paths of unequal length and is recombined on the beam–splitting plate (Fig. 3.25). The path difference creates an interference of the light waves. If the path difference is varied uniformly by moving a mirror at a constant speed, then the intensity varies from bright to dark as the two component beams move in and out of phase. A recording of this intensity output is referred to as the *interferogram* and the spectrum can be reconstructed from the interferogram using

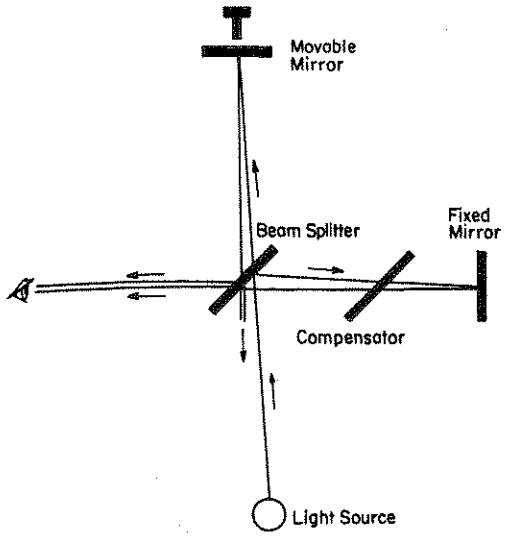

Figure 3.25 The Michelson interferometer splits the incoming light into two beams that travel different distances to the detector. A compensator plate equalizes the optical paths of the two light beams in the glass.

the Fourier transform. In a sense, the interferogram contains all the needed information about the spectrum in a coded form.

Excursus: The Resolving Power of an Interferometer

The elegance of the interferometer arises from the fact that its resolving power is no longer related to the length of the optical path or width of ruled lines on a grating. It is purely a function of the path difference of the two beams. We can appreciate this by considering a Michelson interferometer illuminated by a source of light at two adjacent wavelengths, λ and $\lambda + \Delta\lambda$. As the mirror moves, the bright interference fringes periodically appear, disappear, and then reappear again. If a small displacement of the mirror in its travel is Δx, then we can define the resolution of the instrument $\Delta\lambda$ in terms

of this displacement. Here we consider Δx as the displacement the mirror that causes a one–cycle variation in the visibility of th fringes.

We establish the relationship between Δx and $\Delta\lambda$ in the follow ing way. The fringe visibility is high when bands of λ overlie thos of $\lambda + \Delta\lambda$ and poor when the bright fringes of the former coincid with the dark fringes of the latter. This situation occurs when λ an odd number of half–wavelengths of $\lambda + \Delta\lambda$. For a path of trav $2x$, then the condition of minimum visibility is

$$2x = n_1\lambda = (n_2 + \frac{1}{2})(\lambda + \Delta\lambda)$$

where n_2 are odd integers. Noting that

$$n_1 = \frac{2x}{\lambda}, \qquad n_2 + \frac{1}{2} \approx \frac{2x}{\lambda}(1 - \frac{\Delta\lambda}{\lambda})$$

for $\Delta\lambda \ll \lambda$, then subtraction yields

$$n_2 - n_1 + \frac{1}{2} \approx -\frac{2x\Delta\lambda}{\lambda^2}$$

Suppose now that the integer $n_2 - n_1$ increases by 1 as x goes from x to $x + \Delta x$, and

$$n_2 - n_1 + \frac{3}{2} \approx \frac{2(x + \Delta x)\Delta\lambda}{\lambda^2}$$

If we subtract these two equations and rearrange, it follows that

$$\Delta x \approx \frac{\lambda^2}{2\Delta\lambda}$$

In terms of wavenumber $\tilde{\nu}$, $d\tilde{\nu}/d\lambda = -1/\lambda^2$, and

$$\Delta\tilde{\nu} \approx -\frac{1}{2x}$$

In principle, the path difference Δx can be increased without limit and the resolving power of the interferometer made arbitrarily high. For example, a resolution of 0.1 cm^{-1} is achieved by moving the mirror only 5 cm. We can employ similar arguments to illustrate that the spectral range of the instrument is also broad. In this

the spectral range of the instrument is determined by how finely we resolve the mirror position (however this range is usually practically defined by the spectral range of the detector used in the instrument).

The functioning of the interferometer is illustrated by considering the case when a monochromatic beam such as a laser source enters the instrument. If the moving mirror is adjusted so there is no path difference between the two beams, then the light will appear bright. When the mirror is moved one-fourth of the laser wavelength, the interference beam (i.e., the beam that bounces off the moving mirror) is exactly 180 degrees out of phase with the second beam so that no light is detected. Continuous movement of the mirror along one direction produces an oscillatory signal as the light changes from bright to dark. The form of this signal can be understood by considering two beams

$$\mathcal{E}_1 = \mathcal{E}_o \cos(kx - \omega t)$$

$$\mathcal{E}_2 = \mathcal{E}_o \cos(-\omega t)$$

where the first expression defines the electric field of the laser light for the path defined by the mirror position at x (the interference field) and the second expression applies to the field with the mirror determined to be in the $x = 0$ position (which is equivalent to the field of the second beam). The field combined at the detector has the form

$$\mathcal{E} = \mathcal{E}_1 + \mathcal{E}_2$$

The measured intensity is proportional to the time averaged $\mathcal{E}$ field (Chapter 2)

$$I = < \mathcal{E}^2 >$$

where we omit the proportionality constant and the angle brackets represent the time integral

$$I = \frac{1}{T} \int_t^{t+T} [\mathcal{E}_1^2 + \mathcal{E}_2^2 + 2\mathcal{E}_1\mathcal{E}_2] dt$$

Using arguments presented in chapter 2 in discussion of light intensity, and assuming the product $\omega T >> 1$, it follows that

$$I(x) = I_{o,\tilde{\nu}}[1 + \cos(2\pi x\tilde{\nu})] \tag{3.45}$$

where $I(x)$ is the output signal expressed as a function of the distance of the mirror movement x, and $I_{o,\nu}$ is the source of radiation that enters the instrument.

An interferogram is the output signal that results from the su mation of all the oscillations associated with all wavelengths. T mathematical expression of the interferogram in this case is

$$I(x) = \frac{1}{2\pi} \int_{-\infty}^{\infty} I_{o,\tilde{\nu}} \cos(2\pi x\tilde{\nu}) d\tilde{\nu} \tag{3.4}$$

where it is assumed that the interferences are symmetric about t $x = 0$ position. An example of the interferogram obtained fr measurements of the atmospheric emission by NASA's infrared terferometer spectrometer (IRIS) is shown in Fig. 3.26a. The Ea radiation spectrum is then found by taking the Fourier transform the interferogram

$$I_{o,\tilde{\nu}} = \int_{-\infty}^{\infty} I(x) \cos(2\pi x\tilde{\nu}) dx \tag{3.4}$$

Figure 3.26b provides an example of the optical layout of t IRIS. This instrument was designed to provide information abc the vertical temperature profile, water vapor, and ozone profiles the global scale. Radiation enters the instrument through a mir and is divided nearly equally by the beamsplitter. The instrume is actually two coupled interferometers, with one associated wi light collected from the atmosphere by scanning mirror at the top the instrument and the other for the monochromatic source whi is used to count fringes (refer to Problem 3.13 as an example of t use of this second system).

Figure 3.27 shows the emission spectra obtained from int ferometers flown on different spacecraft. The infrared spectrum Earth, under cloudless conditions, is dominated by the absorptio of water vapor and carbon dioxide. The spectra of both Mars a Venus indicate the importance of CO_2 as a source of gaseous opaci the only major difference is the abundance in CO_2 of nearly 100 instead of the Earth's 330 ppm.

Another example of an interferometer spectrometer is the hi resolution infrared sounder (HIS) developed by the group at U versity of Wisconsin. This instrument has been designed for m teorological applications and measures the infrared emission of t atmosphere with a spectral resolution around 0.1 cm^{-1}. The instr ment uses three detectors to sense the radiation over three bro spectral regions. An example of the output from the instrume is provided in Fig 3.28 which compares coincident spectra obtain

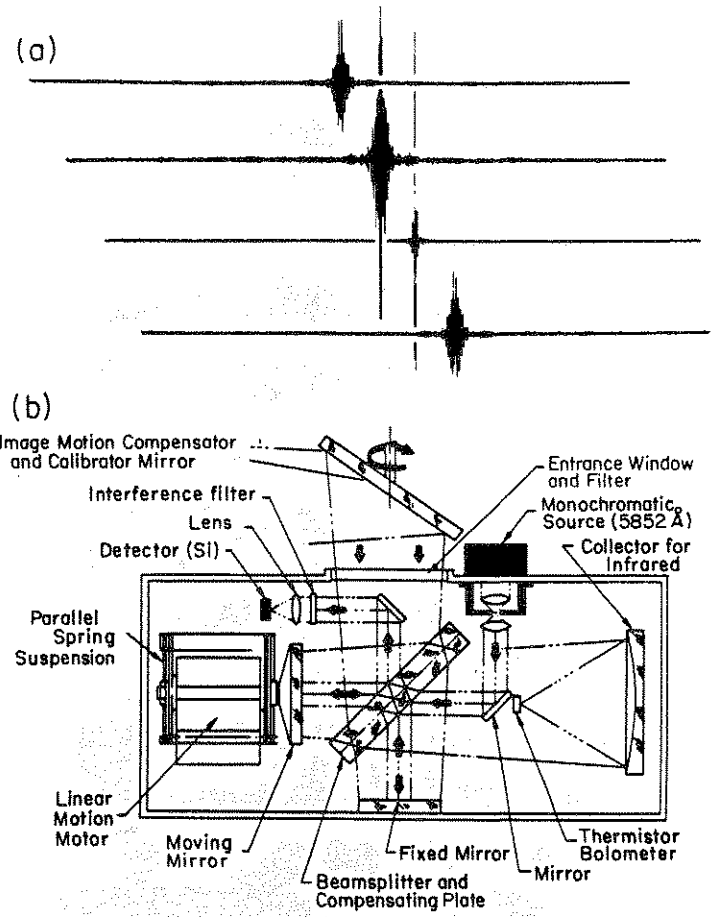

Fig. 3.26 (a) Examples of interferograms measured by the IRIS from space. (b) A schematic of the optical arrangement of the Nimbus IRIS instrument. The spectral resolution of the instrument is 5 cm^{-1}. There are actually two coupled interferometers, with one associated with light collected from the scanning mirror at the top of the instrument, the other for the monochromatic source which is used to count fringes.

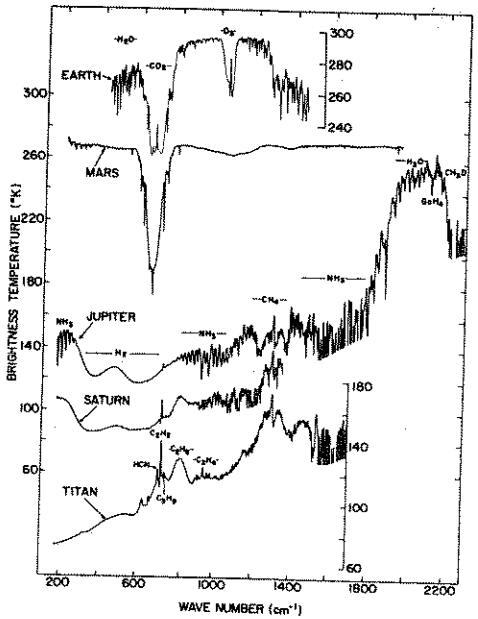

Figure 3.27 Spectrum of the infrared, expressed as brightness temperatures for four planets and Titan (Hanel, 1983).

from interferometers on an aircraft and at the ground. The project at the back of this book elaborates further on the operation of an interferometer and the emission spectra of the atmosphere measured at the ground. Interpretation of the spectra shown in Fig. 3.28 is left for Problem 7.1.

3.7 Notes and Comments

3.1 and 3.2. A wonderful elementary text on molecular spectroscopy is that of Banwell (1983) and the material described in these two sections follows his treatment of the topic.

Molecular absorption has also played a role in understanding the nature of cosmic radiation. Cosmic radiation is a topic relevant to our understanding of the origin of the universe. Radio astronomers

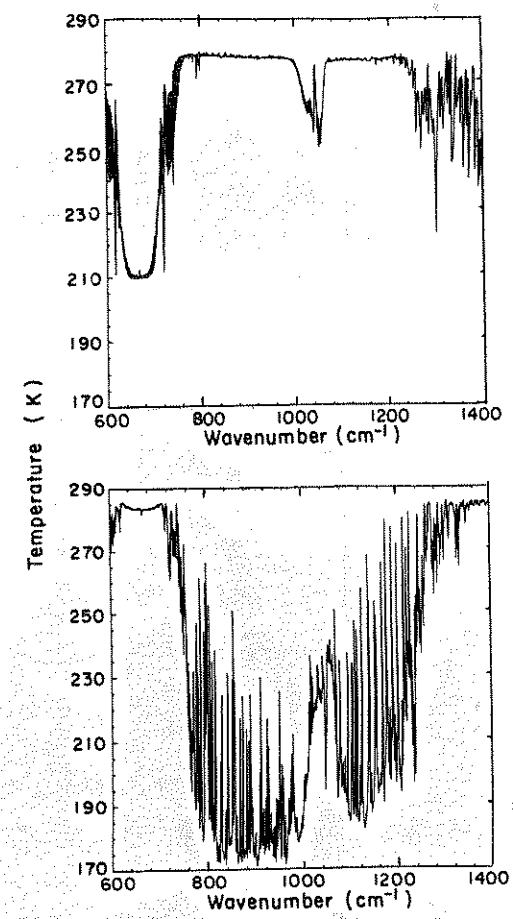

Figure 3.28 Spectra of the infrared emission obtained on March 1991 from the HIS instrument on an aircraft looking down (upper spectrum) and at the ground looking up (lower spectrum) (Smith, personal communication).

matches that of a blackbody with a temperature between 2.7 and 3 K. To establish whether or not this radiation is truly blackbody radiation we need to measure the cosmic radiation at wavelengths shorter than the microwave radiation measured by the radio astronomers to see if the energy density falls off with decreasing wavelength as the Planck function predicts. Unfortunately, the atmosphere of our planet becomes increasingly opaque at wavelengths below 0.3 cm (e.g., Fig. 3.18) and its not possible to estimate cosmic background radiation at wavelengths shorter than 0.3 cm from surface based measurements.

Interestingly enough, the amount of radiation background from space was deduced from measurements at these shorter wavelengths in 1941, long before the measurements by radio astronomers were reported. The background radiation was deduced from optical measurements of the light from the star ζ Oph which belongs to the constellation Ophiuchus ("the serpent bearer"). The light from this star observed at earth shows the existence of dark lines, indicating that a cloud of intervening gas absorbs the radiation. One of the absorption lines in the spectrum of ζ Oph occurs at a wavelength of 0.3875 μm which indicates the presence of the molecule cyanogen (CN). This absorption line is actually split into three lines with wavelengths 0.3874608, 0.3875763, and 0.3773998 μm. The first line corresponds to a transition from the ground state of the CN molecule to a vibrating state and is expected even in a zero–temperature environment. The other two lines could only be produced by transitions in which the molecule is lifted from an existing state of rotation to higher vibrating states. Thus a fraction of the CN molecules must be in this rotating state. From the known energy difference between the ground state and the rotating state, and from the observed relative intensities of the lines, it was deduced that the CN molecule was exposed to some kind of perturbation with an effective temperature of about 2.3 K. Further information about the cosmic background radiation can be found in Wienberg (1977).

3.3 and 3.4. The shape of an absorption line for paths along which pressure and temperature vary is not given by the Lorentz profile for absorption at fixed temperature and pressure. A simple way of thinking of this is to imagine the resulting line profile for a path through two cells in which the pressure and temperature are fixed but differ from one to the other. The profile is a superposition of two different profiles, one narrower than the other. This profile is

broad in the wings due to contributions from the higher pressure cell and narrow and spiked at the center due to the absorption in the cell of lower pressure. In treating the effects of pressure and temperature variations along the path, it is usually assumed that the profile remains closely Lorentzian with parameters adjusted to fit the absorption in the wings and/or in the line center. These approximations are discussed in Goody and Yung (1989).

The shape of the 22 GHz water vapor line, and the matching of simple shape models to laboratory data, is a topic discussed by Walter (1992a). Yasim and Armstrong (1990) provide a theoretical study of the water vapor lines at 183 GHz and for microwave frequencies beyond.

3.5. Over the past decade or so molecular absorption data have been systematically archived. Periodic revisions are reported in the open literature and these data sources are rapidly becoming an 'industry standard'. Two of these compilations are those of the Air Force Geophysics Laboratory (AFGL) and described by Rothman et al. (1987) and another, in many respects, similar compilation has been developed by Chedin and collaborators under the acronym GEISA (Husson et al., 1992).

An abbreviated bibliography of pressure sensing via measurements in the oxygen A band is given at the end of Chapter 6.

An approximate theory of line continuum introduced in the recent work of Ma and Tipping (1992a and b) suggests that the continuum is predominantly the result of overlapping wings of distant self-broadened water vapor lines. Other schools of thought suggest that the absorption mechanism involves two water vapor molecules loosely bonded as a water vapor dimer. However, it appears that this type of absorption requires greater concentrations of dimers than are typically found at ordinary atmospheric water vapor densities. Continuum absorption in the 8–12 μm atmospheric window is important for remote sensing as well as for a number of other meteorological reasons (Burroughs, 1979).

3.6. A classic treatise on microwave spectroscopy is that of Townes and Schalow (1955). There are several ways to measure the emission spectra at microwave frequencies with enough spectral resolution to distinguish the absorbing species of interest. For example, one approach is the total power radiometer (Decker et al. 1978) which detects radiation using a parallel bank of channels, one for each frequency required. An alternative approach is the autocorrelation

radiometer which provides highly resolved spectral absorption information at microwave frequencies using techniques that are directly analogous to interferometry (Ruf and Swift, 1988).

A useful text on the subject of spectrometry as it is used in satellite instrumentation is that of Chen (1985). A general reference text on interferometry is that of Hariharan (1990).

3.8 Problems

3.1. Briefly explain or interpret the following:

a. Two sealed chambers contain the same amount of water vapor and are at the same temperature. One contains only water vapor while the other holds a mixture of water vapor and air. Which has the smaller transmissivity averaged over a narrow spectral region containing a single water vapor absorption line?

b. The two sealed cells of (a) now both contain some amount of water vapor mixed in air. The concentration of water vapor in one cell is adjusted so that the transmission of $10\mu m$ radiation through one cell matches the transmission of $6.3\mu m$ radiation through the other cell. Which cell contains the most water vapor?

c. The temperature of both cells is now increased thus raising the pressure within the cell but assume no other changes occur. At which wavelength is the transmission a maximum (ignore any temperature effects on absorption)?

d. Molecules possessing a permanent electric dipole (known as polar molecules) readily absorb at infrared wavelengths. Molecular oxygen is not an electrically polar molecule but also has infrared and microwave absorption lines.

e. The rotational–vibrational spectra of CO_2 exhibits absorption lines that are regularly spaced whereas absorption lines of H_2O are more randomly distributed in the spectrum.

3.2. The wavelength of radiation absorbed during a particular spectroscopic transition is observed to be 10 μm. Express this in frequency (Hz) and in wavenumber (cm^{-1}) and calculate the energy change during the transition in both joules per molecule and joules per mole. If the energy were twice as large, what would be the wavelength of the corresponding radiation? *Hint*: Planck's constant has the value h =6.63 $\times$ 10^{-24} joules s molecule^{-1}. Avagadro's number N= 6.02 $\times$ 10^{23} mol^{-1}.

where e is the partial pressure of water vapor, p is the partial pressure of dry air, T is the absolute temperature, the parameters k_i at a given wavelength are constants, and $z_{a,w}$ represent deviations from the ideal gas law (Owens, 1967). This refractive index depends on the humidity of the air and so the propagation of the pulse also depends on the humidity. This dependence is actually important for some remote sensing applications and is explored further in Problem 4.6.

An interesting application of (4.19) is described by Keeling (1988) who proposed that the relationship between refractive index and concentration could be used to measure small changes in the mole fraction of oxygen in air. Measurement of this fraction is extremely difficult but it is an important measurement in the study of the CO_2 budget of the atmosphere. Keeling's approach requires measurement of small changes in the refractivity of dry air at two wavelengths. The parameter relevant to his analysis is the refractivity ratio

$$r = \frac{\mathrm{m}(\lambda_1) - 1}{\mathrm{m}(\lambda_2) - 1}$$

and it follows from (4.20) that this ratio varies with species abundance according to

$$\delta r = s_i \delta y_i \tag{4.21}$$

where

$$s_i = \frac{\mathrm{m}_i(\lambda_2) - 1}{\mathrm{m}_{air}(\lambda_2) - 1} \frac{r_i - r_{air}}{1 - y_i}$$

In deriving (4.21), Keeling assumes that the change in mole fraction δy_i of species i occurs in such a way that the relative abundances of all other species (i.e., the ratios y_j/y_k where $j, k \neq i$) remain constant. Measurement of the changes in r in dry air corrected for changes in CO_2 and other gases then yield the change in mole fraction of O_2. To measure the change in refractivity ratio δr, Keeling designed a novel interferometer illuminated by an Argon lamp filled with a trace of ^{198}Hg for which the positions of two lines at 4360 and 2537 Å are known to within 0.0001 Å. The refractivity is determined from the optical path difference between beams that pass through two cells, one filled with the flowing air sample and one filled with a reference gas. By combining these beams at a recombining plate, the path difference in the interferometer is determined by counting fringes formed by the interference of the beams. Keeling proposes that this approach is capable of yielding changes in the mole fraction

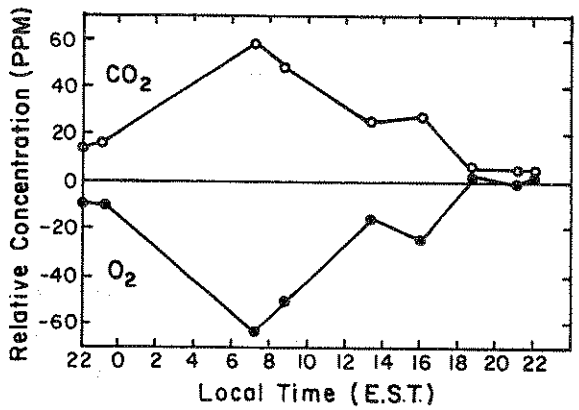

Figure 4.11 Diurnal trend in oxygen and carbon dioxide. The data are expressed as a difference between ambient air and a reference gas. The approach to near background levels of both gases after 1800 local time is due to the mixing by strong winds associated with the passage of a storm system (Keeling, 1988).

of oxygen with a precision of ±2 ppm and used this measurem approach to show how changes in O_2 are anticorrelated with C which is expected for combustion processes (Fig. 4.11).

4.4 Reflection and Transmission at a Plane Boundary

Packing oscillators in dense materials like solids and liquids, in c trast to gases, dramatically impacts on the way radiation intera with this type of matter. To appreciate how the arrangement dipoles in bulk matter affects these interactions, it is useful to c sider the reaction of electromagnetic radiation with a regularly ranged, large number of oscillators. We consider these reactions h in the context of reflection and transmission at a plane interfa This is more than a tutorial exercise as reflection and transmiss properties of homogeneous slablike materials are widely used in mote sensing of land and ocean surface properties.

4.4.1 Propagation in a Homogeneous Slab

Every oscillator influenced by incident radiation emits an electromagnetic wave. Because the oscillators are packed together in a homogeneous slab, these emitted waves (which we refer to as "secondary waves") interfere with each other and with the incident wave in a very orderly way. For example, the wave incident on a slab of water is completely cancelled by interference with these secondary waves and is replaced by a wave which propagates along a direction that is different from the original incident direction. The individual emissions from the dipoles build up a wave referred to as the *refracted* wave propagating in a forward direction (i.e., into the material) and a wave referred to as the *reflected* wave propagating in a direction away from the material.

The refracted wave also travels in matter with a speed v which is different than the ordinary velocity of light c. One conceptual interpretation of refraction is offered by Huygens, who considered the wave front to slow down as it enters the slab, ultimately altering its direction of propagation (Fig. 4.12). The distance between wave fronts in water is shorter than in air, and this distance is proportional to the respective refractive indices. As we shall see in Chapter 5, the actual change in phase of the wave in a particle also gives rise to interference effects which dominate the way radiation reacts to the presence of particles.

Refraction at a plane surface is described in terms of an approximate relation referred to as *Snell's law of refraction* that can be simply written as

$$\frac{\sin\theta_i}{\sin\theta_r} = \frac{v_1}{v_2} = m_{21} \tag{4.22}$$

where θ_i and θ_r are the angles of incidence and refraction, respectively, relative to the surface normal, and v_1 and v_2 are the speeds of the wave in medium 1 and medium 2. The ratio of the speeds of the wave m_{21} is the relative refractive index, which indicates the relative difference in the speeds of the wave in medium 2 to medium 1. In a vacuum, v_1 is simply the speed of light, $m_1 = 1$ and $m_{21} = m_2$.

In describing the properties of the reflected wave, we need to consider a thin layer of oscillators near the surface (about as deep as half a wavelength). In this thin layer, the radiation scattered in the back direction (i.e., in a direction opposite to that of the incoming wave) is not completely cancelled by interference. The scattered

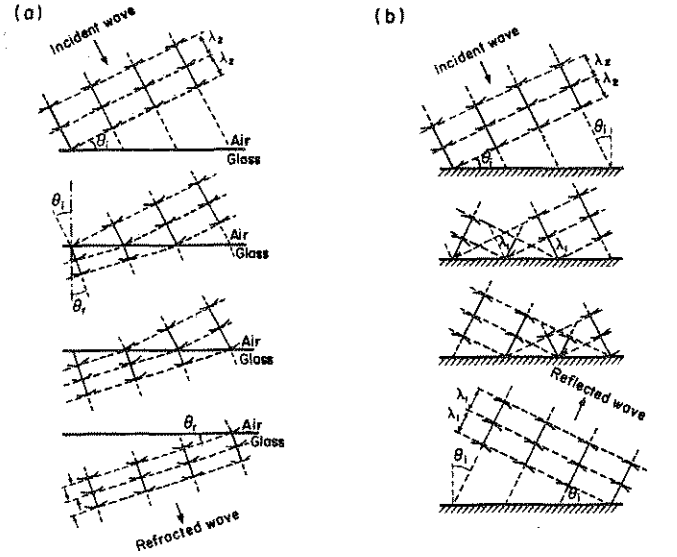

Figure 4.12 (a) Refraction and (b) reflection of plane waves at an interface with ($m_2 > m_1$).

waves superimpose to produce the reflected wave, which is also related to the refractive index of the material. We arrive at such a relationship in the following way. Consider an electromagnetic wave incident on a plane boundary as shown in Fig. 4.13. In describing the reflection and refraction of this wave it is convenient to think of each field as having a component parallel and perpendicular to the plane of reference. Maxwell's equations provide certain relations among the parallel and perpendicular components of the electric and magnetic fields on both sides of the interface. From these relationships, and by matching the components at the interface, reflection (and transmission) coefficients can be derived (e.g., Born and Wolf, 1964). These coefficients are

$$r_\ell = \frac{m_1\cos\theta_r - m_2\cos\theta_i}{m_1\cos\theta_r + m_2\cos\theta_i}$$

$$r_r = \frac{m_1 \cos\theta_i - m_2 \cos\theta_r}{m_1 \cos\theta_i + m_2 \cos\theta_r}$$

$$t_\ell = \frac{2m_1 \cos\theta_i}{m_1 \cos\theta_r + m_2 \cos\theta_i}$$

$$t_r = \frac{2m_1 \cos\theta_i}{m_1 \cos\theta_i + m_2 \cos\theta_r} \qquad (4.23)$$

We now define the *reflectivity* and *transmissivity* as coefficients for the energy reflected and transmitted at the interface rather than as coefficients that relate to the reflection and transmission of wave amplitudes. The reflectivities for intensities are

$$\mathcal{R}_r = |\, r_r \,|^2$$

$$\mathcal{R}_\ell = |\, r_\ell \,|^2 \qquad (4.24)$$

For an opaque slab, the emissivities are

$$\varepsilon_r = 1 - \mathcal{R}_r$$

$$\varepsilon_\ell = 1 - \mathcal{R}_\ell. \qquad (4.25)$$

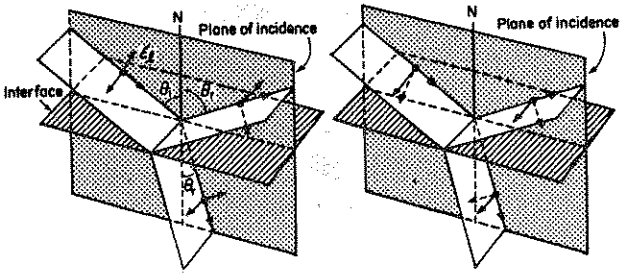

Figure 4.13 The electric fields of incident, reflected, and refracted waves relative to the plane of reference for the two polarization components.

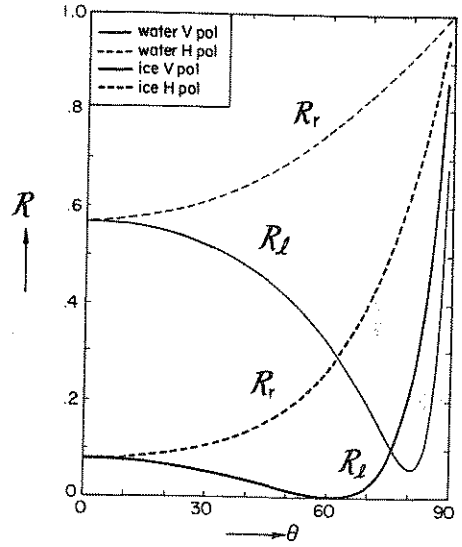

Figure 4.14 Reflection coefficient of water and ice at 19GHz. The angle corresponding to a zero parallel component is the Brewster angle.

There is one very important consequence of (4.23). Unpolarized waves incident on a homogeneous layer of material can become partially or totally polarized on reflection. In the example of microwave radiation, a portion of the unpolarized radiation emitted from the atmosphere is reflected by the ocean surface by an amount determined by (4.24), and another portion of this atmospheric radiation is absorbed and subsequently re–emitted by the ocean to the atmosphere. The components of this oceanic microwave emission are given by (4.25). Therefore, the amount of radiation emitted with a perpendicular polarization state is different from the component emitted with a parallel component for a plane water surface when viewed at an oblique angle. This property provides a way of discriminating surface water from rainfall in the microwave.

Figure 4.14 shows the amplitudes of the reflection coefficients for water as a function of incident angle. These were calculated using (4.23) and (4.24) with values of m at 19 GHz for both water

and ice surfaces. According to these formulas, there is one special case corresponding to the situation in which $r_\ell = 0$, that is the reflected wave has no component parallel to the incident plane. This occurs when the direction of this would–be parallel component parallels the direction of the incoming beam. Since there is no oscillation along the latter direction, the reflected component can have no oscillation in this direction. According to (4.23), this happens when $m_2 \cos\theta_i = m_1 \cos\theta_r$. Using Snell's law, we obtain the condition that $\theta_i + \theta_r = \pi/2$ for the case of total polarization, and θ_i is referred to as *Brewster's angle* or the *polarizing angle*.

Another consequence of polarization by reflection, and one exploited in the design of certain types of systems (such as in some lidar systems), is that when circularly polarized light is incident on the slab, the reflected light is also partially circularly polarized but in the opposite sense. Right–handed polarized light transmitted from an instrument arrives back left–handed after reflection from particles in the atmosphere. In a lidar system as shown in Fig. 4.15, parallel–polarized light from the laser is transmitted directly through a transmit/receive (T/R) switch which is a plate oriented relative to the beam at the Brewster angle (assuming the plate is lossless). The beam transmitted to the atmosphere is first made circularly polarized by passing it through a quarter wave plate. The scattered radiation returns circularly polarized but with opposite handedness. This light, when passed through the same quarter wave plate, is transformed to perpendicularly polarized light, which is then reflected by the T/R switch into another part of the instrument for detection and further analysis.

4.4.2 Attenuation of Radiation in a Homogeneous Slab

In our discussion of oscillating dipoles we view absorption as a kind of dampening process. We will now consider the issue of absorption in the context of wave propagation. The general expression for a propagating wave is written in the form

$$\mathcal{E} = \mathcal{E}_o e^{i(\vec{k}\cdot\vec{r}-\omega t)} \tag{4.26}$$

where in a slab of condensed matter

$$\vec{k}\cdot\vec{r} = m\vec{k}_o\cdot\vec{r} \tag{4.27}$$

which is defined relative to the wavenumber $\vec{k}_o$ in a vacuum. Since m is complex in an absorbing slab, $\vec{k}$ too is complex. For the simplest

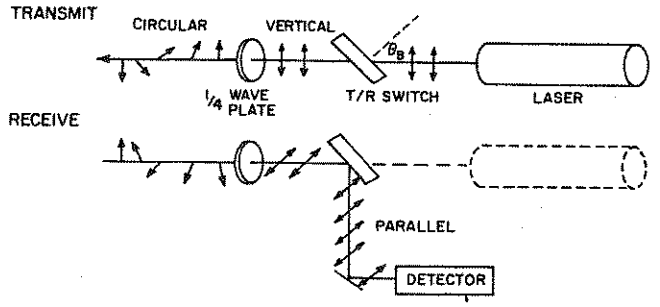

Figure 4.15 A simplified optical arrangement of a transmit/receive switch which uses the properties of light in a slab at Brewster's angle to discriminate between transmitted and returned light. Light is transmitted totally in one direction and reflected when entering from the other direction because of change in the handedness of polarization by particle scattering.

case of plane wave propagation along the z direction and with $m = n + i\kappa$ in (4.27), equation (4.26) may be written as

$$\mathcal{E} = \mathcal{E}_o[e^{-2\pi\kappa z/\lambda_o}]e^{i(n\vec{k}_o z-\omega t)} \tag{4.28}$$

The first of the exponential factors describes the rate at which the radiation is attenuated in the slab. The second exponential factor represents the oscillatory part of the wave and we observe that the real part of the refractive index determines the phase speed of the wave. The attenuation factor can be written in terms of a bulk absorption coefficient $\varrho = 4\pi\kappa/\lambda_o$ such that the attenuation of intensity of the radiation is

$$I = I_o e^{-\varrho z} \tag{4.29}$$

A useful and convenient way to interpret this attenuation is in terms of the penetration depth $d_I = 1/\varrho$, is the depth to which the incident intensity is reduced by $1/e$.

4.5 Selected Applications of Surface Remote Sensing

For practical reasons, the focus of this book is directed toward the remote sensing of the atmosphere. Appreciation of the importance of the ocean and its coupling to the atmosphere has loomed as one of the major developments in atmospheric research over the past two decades.[3] The advent of the Seasat–A and Nimbus 7 satellites, both launched in 1978, opened up new opportunities for evaluating various radiometric techniques for monitoring the ocean surface from space. Two applications that exploit the differences in the microwave optical constants of both water and ice will now be described.

4.5.1 Monitoring Sea Ice Extent

One of the more useful consequences of the large emissivity difference between ice and water in the microwave (the real parts of the dielectric constants are approximately 3 and 80, respectively) lies in its application to mapping sea ice. Understanding the variability and extent of sea ice is considered important to understanding climate variability.

To illustrate how sea ice is mapped using passive microwave measurements, consider the case of microwave radiation upwelling from the atmosphere at an angle θ. The equivalent microwave temperature for the given polarization state ℓ or r of such a (natural) surface can be expressed for a general observation angle θ as[4]

$$T_{\ell,r}(\theta) = \mathcal{T}r(\theta)[(1 - \mathcal{R}_{\ell,r}(\theta))T_{ocean} + \mathcal{R}_{\ell,r}(\theta)T_{sky}] + T_{sky} \tag{4.30}$$

where $\mathcal{T}r$ is the transmission through the atmosphere along θ, and T_{ocean} and T_{sky} are the temperatures associated with emission from the ocean surface and atmosphere, respectively. The first term is

[3] The Tropical Ocean Global Atmosphere (TOGA) Program is a program under the auspices of the World Climate Research Program (WCRP) which focuses on improving the medium to long–range predictions of the tropical ocean–atmosphere system, including the El Nino–Southern Oscillation. One of the problems that emerged from TOGA was an appreciation of the complexity of the coupled system over the warm pool region of the equatorial west Pacific Ocean.

[4] A more complete derivation of this equation is presented in Chapter 7.

the emission from the surface, the second is the reflection of the sky emission at the surface, and the last term is the direct emission from the atmosphere to a sensor on a satellite.

Consider two adjacent surfaces, one referred to by the subscript i (ice) and the other by the subscript w (water). The temperature contrast between these surfaces (neglecting reference to polarization) is

$$\Delta T = T_i - T_w = (\mathcal{R}_i - \mathcal{R}_w)\,(T_{sky} - T_{water}) \tag{4.31}$$

where for simplicity we take $\mathcal{T}r \approx 1$. It follows from (4.23) and (4.24) that for vertical incidence

$$\mathcal{R}_{i,w} = \left| \frac{\mathrm{m}_{i,w} - 1}{\mathrm{m}_{i,w} + 1} \right|^2 \tag{4.32}$$

and assuming typical values of m for ice (m$=\sqrt{3}$) and water (m $=\sqrt{80}$), it follows that

$$\Delta\mathcal{R} = \mathcal{R}_w - \mathcal{R}_i = 0.57.$$

Given this estimate, together with values $T_{sky}(\approx 50K)$ and $T_i(\approx 273K)$, we then obtain $\Delta T \approx -127K$. Thus, the water surfaces appear substantially darker than the more emissive ice surface. It is this basic difference in the emission of water and ice that is used in satellite monitoring of sea ice.

Microwave brightness temperature distributions over the southern polar regions for four months of the year are shown in Fig. 4.16. In the ice covered area, the changes in brightness temperature are mainly due to changes in the nature and composition of the ice. In fact, sea ice is quite a complex dielectric material. Its composition includes all three phases of matter: a solid phase consisting of ice crystals and salt precipitates; a liquid phase consisting of brine solution; a gaseous phase in the form of air pockets in the ice.

Changes in the composition of sea ice occur continuously, producing changes in the optical properties of ice. Certain ice types have been identified as having distinguishable radiometric signatures: new ice, first–year ice, multiyear ice, and summer ice. A basic difference between first–year ice and multiyear ice is the presence of brine in the former and the replacement of brine by air pockets in the latter. The change in dielectric properties of ice associated with this change in composition produces radiometric effects such as that presented

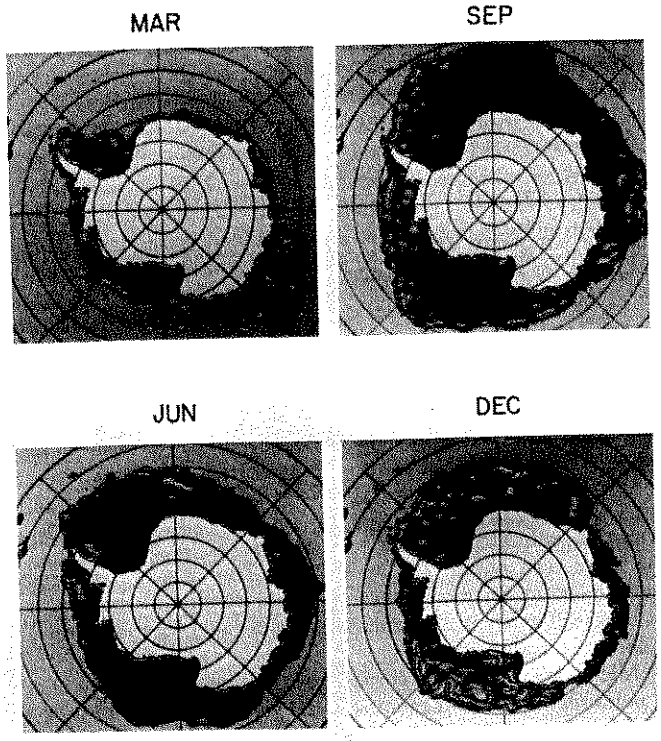

Figure 4.16 The extent of Antarctic sea ice varies from season to season. The satellite microwave images for the four months clearly show the minimum sea ice extent in March and the maximum sea ice extent in September. The grayscale variations represent different brightness temperatures due to different ice composition and thus age of the ice (from Gordon and Comiso, 1988).

this ice appears warmer than multiyear ice, especially for frequencie exceeding 30 GHz. This difference is further exaggerated by the ai bubbles in multiyear ice. These increase the forward scattering c microwave radiation in multiyear ice, especially at 31 GHz as show in Fig. 4.17a, leading to decreased values of brightness temperature Tooma et al. (1975) used the multispectral behavior of brightnes temperature as a means of discriminating different types of ice. The proposed an identification procedure based on a cluster approach i which temperature differences measured at two frequencies are cor related in the manner shown in Fig. 4.17b.

4.5.2 Measurement of Near—Surface Wind Speed

We know from observational experience that the microwave bright ness temperature measured above a wind roughened water surfac increases in a somewhat systematic way with increasing wind speed This observation forms the basis for deriving wind speed from mi crowave brightness temperature data. However, the brightness tem peratures are only an indirect indication of wind speed and the phys ical basis for the retrieval of surface wind is not firmly established.

A water surface becomes sloped when it is roughened by wind and the direction of the reflected and refracted radiation at the sur face is therefore tilted according to the amount of surface slope This is what alters the brightness temperature of the surface and i has been empirically deduced that the amount of sloping of a wind roughened ocean surface varies according to the wind speed. Co and Munk (1955) demonstrate that the full range of slopes of wave is empirically specified by a Gaussian distribution with a variance

$$\sigma_{CM}^2 = 0.003 + 0.0048v \qquad (4.33$$

where v is the wind speed in meters per second defined at a 2 m height above the sea surface. Cox and Munk use visual dat to determine wave slopes so we might expect that only the mor sloped surfaces influence microwave radiation. The slope varianc corresponding to these longer wavelengths is therefore expected to b less than that determined by Cox and Munk from visible radiation Wilheit (1979) empirically deduced that

$$\sigma_\nu^2 = (0.3 + 0.02\nu)\sigma_{CM}^2 \quad \nu < 35\text{GHz}$$

$$\sigma_\nu^2 = \sigma_{CM}^2 \quad \nu \geq 35\text{GHz} \qquad (4.34$$

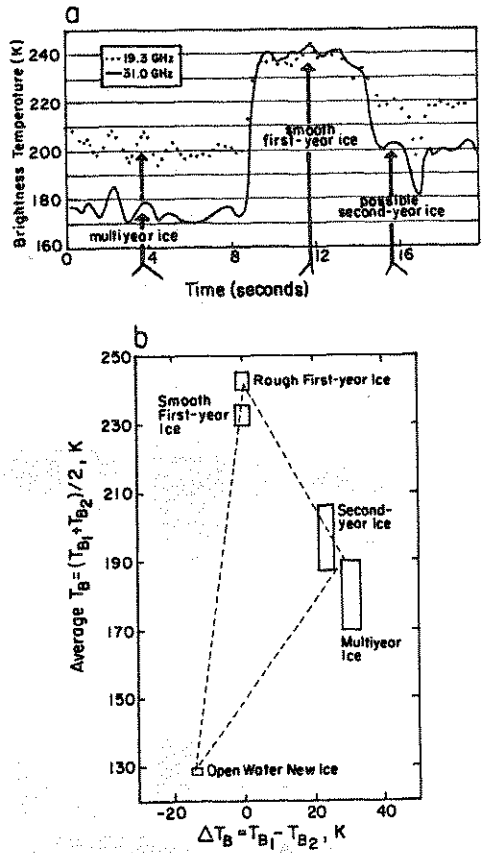

Figure 4.17 (a) Passive microwave profiles for possible second-year ice, smooth first-year ice, and multiyear ice obtained from radiometer measurements as the instrument was flown over an ice surface (from Tooma et al., 1975). (b) A plot of the brightness temperature averaged for two frequencies versus the temperature difference. The nadir brightness temperatures are measured at 19.3 GHz and 31 GHz, respectively (from Tooma et al., 1975).

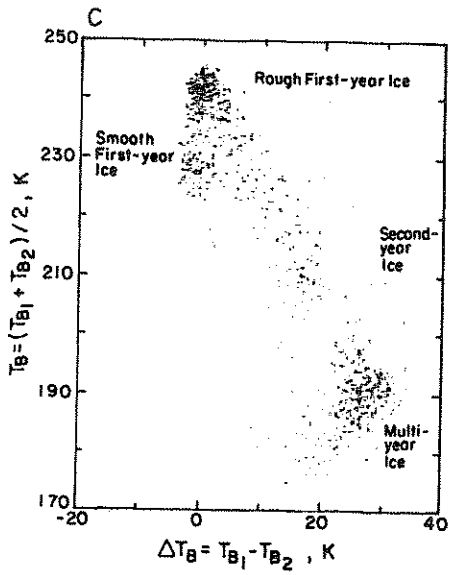

Figure 4.17 (Cont.) (c) An example of the data of (a) clustered on the bispectral diagram drawn in (b) (from Tooma et al., 1975).

With this information about wave slopes, the reflectivity of a rough surface is obtained simply by averaging the Fresnel relations over the distribution of wave slopes. We will not discuss this derivation in detail here, but we will examine a relatively simple method developed by Wilheit (1979). Consider our simple model of the interaction of microwave radiation at the surface as expressed by (4.30). On rearrangement, we obtain

$$\mathcal{R}_{\ell,r}(\theta)[T_{sky} - T_{ocean}] = T_{\ell,r}(\theta) - T_{ocean} \tag{4.35}$$

when $T_{sky} = [1 - Tr(\theta)]T_{ocean}$ and the ratio of two polarization measurements is

$$\mathcal{F} = \frac{T_r - T_{ocean}}{T_v - T_{ocean}} = \frac{\mathcal{R}_r}{\mathcal{R}_v} \tag{4.36}$$

A priori knowledge of the sea surface temperature and measurement of the parallel and perpendicular components of the polarized radiation upwelling from the surface provides us with an estimate of the surface reflectivity ratio. For a perfectly smooth slab observed slightly off Brewster's angle (say at 50 degrees), $\mathcal{R}_\ell < \mathcal{R}_r$ and $\mathcal{F} > 1$. As the surface roughens, $\mathcal{R}_\ell$ increases because this reflection now includes reflections associated with a range of angles defined over a spectrum of sloped wave surfaces. The quantity $\mathcal{F}$ is a measure of surface roughening and thus wind speed. Since it is a ratio, $\mathcal{F}$ is also independent of foam effects which are described shortly. Data from a microwave radiometer have been analyzed in this empirical way and compared to wind speeds measured by operational buoys. The results of this comparison are presented in Fig. 4.18, together with the relationship predicted using the Cox and Monk sea surface slope model (dashed curve). The approach is then to use the measured brightness temperatures and some value of the sea surface temperature to estimate $\mathcal{F}$ and then deduce the wind speed from the relation depicted in Fig. 4.18

Very strong winds also produce foam on the ocean surface and the emissivity and reflectivity of the surface is thus altered depending on the fraction of the surface covered by foam. The measured brightness temperature is found to increase with wind speed in a linear fashion as v exceeds about 7 ms^{-1}. This increase is thought to be largely due to the effects of foam on surface reflection. A number of models varying in complexity have been introduced to deal with the effects of foam on emissivity. Wilheit (1979) provides a simple, albeit empirical, representation of surface reflectivity according to

$$f = 0.006(1 - e^{\nu/7.5})(v - 7), \quad \text{for} \quad v \geq 7 \text{ ms}^{-1}$$

$$f = 0 \quad \text{for} \quad v < 7 \text{ ms}^{-1} \tag{4.37}$$

where ν is in GHz. This function represents the amount by which the surface reflectivity is reduced by foam. In the context of this model the emissivity of the partially covered surface is

$$e_{\ell,r} = 1 - \mathcal{R}_{\ell,r}[1 - f] \tag{4.38}$$

where the effects of roughness are included through $\mathcal{R}_{\ell,r}$ and the effects of foam through f. Here the effects of foam are assumed to be independent of polarization so that $\mathcal{F}$ remains independent of the amount of foam cover.

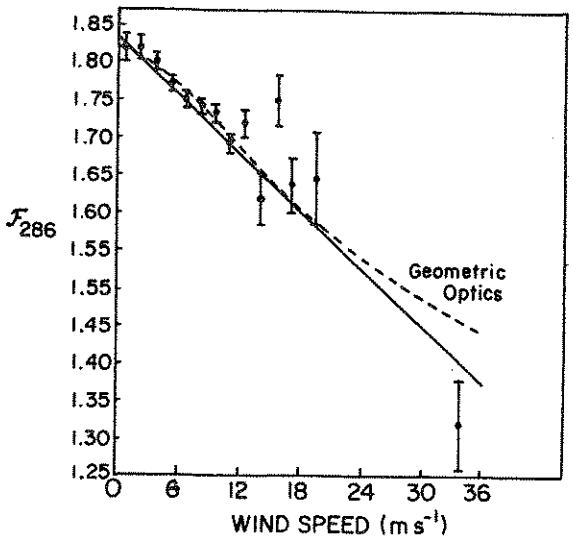

Figure 4.18 Observed values of the reflectivity ratio $\mathcal{F}$ as a function of wind speed. The relationship predicted by the Cox and Munk wave slope model is also shown by the dashed curve and a simple linear regression is given by the solid curve (Wilheit, 1979).

Excursus: Reflection from surfaces— Bidirectional Reflection Functions

Atmospheric remote sensing methods based on measurements of reflected sunlight require information about the reflection properties of the underlying surface. To set the stage for later discussion, these surface properties are introduced using the geometrical framework illustrated in Fig. 4.19. A surface is illuminated with a collimated beam of radiation of flux density F_o which is measured on the surface perpendicular to the direction of flow. For a flux F_o incident on a horizontal surface at an angle θ_o, the incident irradiance at the surface is $F_o \cos\theta_o$. An amount of this radiation is reflected by the surface along the direction $\vec{\xi}$ and confined to the solid angle $d\Omega$. We

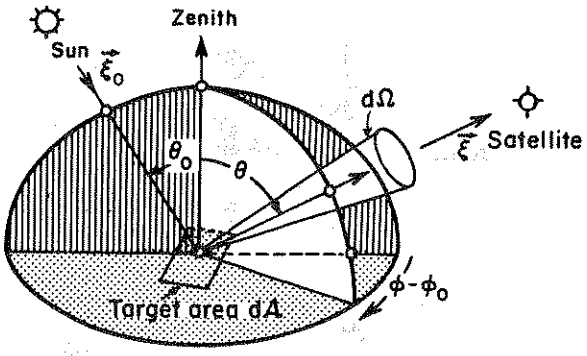

Figure 4.19 Radiation of flux density F_o incident at an angle θ_o on an area element dA and reflected into a solid angle $d\Omega$ along the direction $\vec{\xi}$ which is defined in terms of the zenith angle θ and the azimuth angle ϕ_r defined relative to the azimuth of the sun.

also note here [5] how $\vec{\xi}$ may be represented in terms of the polar angle θ and the azimuth angle ϕ.

If $I(\vec{\xi})$ is the intensity of the radiation reflected from the surface along the direction $\vec{\xi}$ and F_o is the incident flux density, then

$$R(\vec{\xi},\vec{\xi}_o) = \pi I(\vec{\xi})/F_o \cos\theta_o$$

defines a surface reflectivity factor that is a function of two directions; the directions associated with incidence and reflection. This reflection function is sometimes referred to as the *bidirectional reflection function* (BDRF) or alternatively as an anisotropic reflection function. This function is a particularly important parameter in the analysis of satellite radiance data. For example, we need to know $R(\vec{\xi},\vec{\xi}_o)$ for all satellite observation angles $\vec{\xi}$ and all sets of incident solar angles $\vec{\xi}_o$ in order to convert the satellite measurement into a hemispheric flux measurement. Models of $R(\vec{\xi},\vec{\xi}_o)$ for a variety

[5] A more detailed discussion of the directional vector $\vec{\xi}$ and its relation to the angular pair (θ, ϕ) is given in Appendix 1.

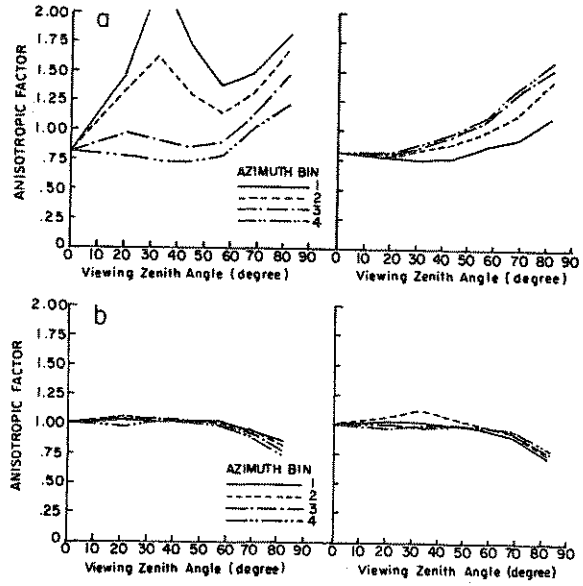

Figure 4.20 (a) The ERBE BDRF of a clear ocean scene as a function of viewing zenith angle for solar zenith angles between 25.84 and 36.87 degrees for eight azimuth angle bins (in degrees) defined as bin 1: $0 < \phi_r < 9$, bin 2: $9 < \phi_r < 30$, bin 3: $30 < \phi_r < 60$, bin 4: $60 < \phi_r < 90$, bin 5: $90 < \phi_r < 120$, bin 6: $120 < \phi_r < 150$, bin 7: $150 < \phi_r < 171$, bin 8: $171 < \phi_r < 180$. (b) Same as (a) but for a clear snow surface.

of surfaces (that is for a variety of different scenes) have been co
structed for this purpose as part of the Earth Radiation Budg
Experiment (ERBE) analysis method.

Figure 4.20 presents the BDRF of two surface types constructe
from a large number of satellite radiance observations obtained f
a given range of solar zenith angles. The reflection function is pr
sented as a function of the viewing angle θ, for eight sets (bins)
azimuth angles ϕ_r. The large values of the BDRF over clear ocear

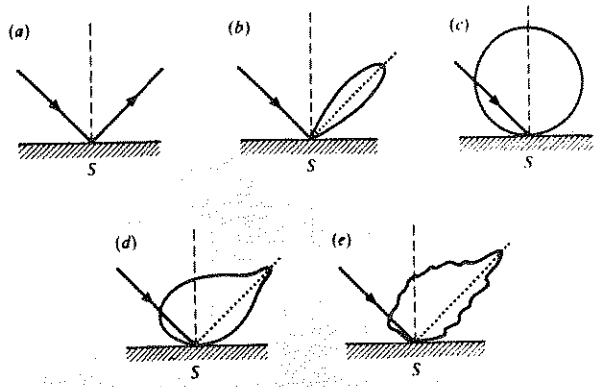

Figure 4.21 A schematic of various types of surface reflection expressed in the form of polar diagrams. The length of an imaginary line joining the point S on the surface to the lobe is proportional to the reflected intensity: (a) specular, (b) quasi–specular, (c) Lambertian, (d) quasi–Lambertian, and (e) complex.

(Fig. 4.20a) for bins 1 and 2 around the view angles of 30 degrees are a result of the sunglint on the ocean surface. Another feature of the ocean BDRFs is the limb brightening (i.e., the increase in reflectivity) toward the horizon when viewed away from the sun (bins 5 to 8). The BDRFs corresponding to snow surfaces are shown in Fig. 4.20b. The angular reflection properties of snow are seen to be more uniform than are the angular reflection properties of water.

We will now consider the BDRFs for two special surface types, the *specular reflector* which is perfectly smooth, and the *Lambertian reflector* which is perfectly rough. These are two important limiting cases of surface reflection. The specular reflector has the property that if the radiation is incident along the direction (θ_o, ϕ_o), then it will be reflected only into the direction $\theta = \theta_o$ and $\phi = \phi_o - \pi$. In this case, the BDRF is expressed by a delta–function as shown schematically in Fig. 4.21a. The ERBE BDRF for an ocean surface is more like Fig. 4.21b which we might consider to be a quasi–specular reflector. The Lambertian reflector represents the case of isotropic reflection from a surface (Fig. 4.21c). In this case the BDRF is defined by a constant value of unity and the ERBE BDRF for a snow surface closely approximates Lambertian reflection.

Excursus: Spectral Reflectance Properties of Land Surfaces

In addition to the angular characteristics of reflected sunlight, the spectral properties of surface reflection also contains useful information about the surface. Unfortunately, the land surface is a highly complex boundary, and so it follows that the spectral properties of that boundary are much harder to define than is the relatively simple case of the ocean surface. The Earth's surface can be heterogeneous in character covered by almost any combination of rocks and sand, grass and vegetation, swamps, mud, and water. The coverage of various types of surface material influences the spectral properties of the surface. Discussions of the spectral properties of the surface can be found in numerous references, some of which are cited at the end of this chapter. Because the land surface is so highly variable in character, analysis of its spectral properties tends to involve a large amount of empiricism; it is beyond the scope of this book to provide a detailed overview of this research.

Instead we focus on the visible and near–infrared spectral properties of certain types of vegetation. An important characteristic of the reflection by vegetated surfaces is the sharp transition in the reflection spectra at a wavelength of about 0.7 μm. Figure 4.22a presents an example of the reflection from corn, soybean, and bare soil. The presence of chlorophyll in vegetation leads to strong absorption at wavelengths shorter than 0.7 μm; the green color of vegetation arises from the rapid rise in the reflectivity in the green portion of the spectrum which continues into the near infrared. The amount of green biomass also affects the reflectance signature at wavelengths greater than 0.7 μm. Figure 4.22b illustrates this feature and presents the spectral reflectance of alfalfa at different stages of its life cycle. The bare field signature corresponds to the zero biomass curve.

A characteristic property of the reflection spectra of vegetation, namely the rapid change with wavelength near 0.7 μm, can be usefully represented in terms of an index

$$\mathrm{NDVI} = \frac{I(NIR) - I(VIS)}{I(NIR) + I(VIS)} \tag{4.39}$$

which is referred to as the normalized difference vegetation index (NDVI) and is an index of biospheric activity more so than as a measure of vegetation amount. In the definition of this index $I(NIR)$

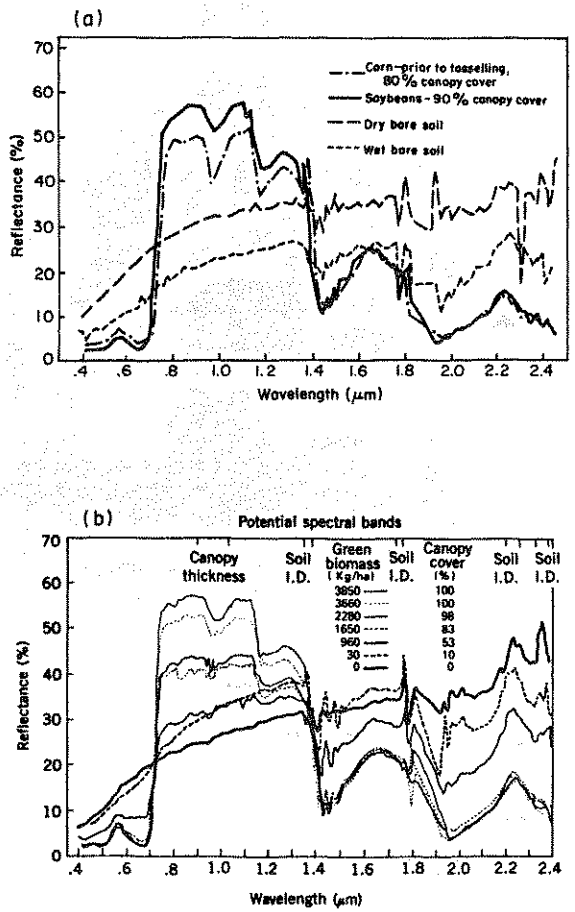

Figure 4.22 (a) The green edge in the reflectance spectrum of vegetation compared to reflection of dry and wet soils. (b) Progressive changes in the spectral response of a surface as the amounts of green biomass and percentage of canopy cover are changed (Short, 1982).

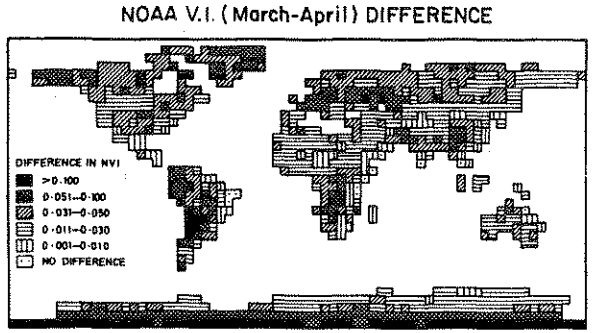

Figure 4.23 Global distribution of the absolute difference between the NDVI on a $5^\circ \times 5^\circ$ grid derived from the NOAA AVHRR satellite data for two consecutive months (from McGuffie and Henderson–Sellers, 1986).

and $I(VIS)$ are the intensities of sunlight reflected at a near–infrare and a visible wavelength, respectively. In this way, the NDVI ca be used to relate the intensities measured by a satellite sensor t the amount of live vegetation in the field of view of the space sensor Figure 4.23 is an example of a satellite archive of the NDVI. The ma shows the absolute difference between the values of NDVI taken fro a seven–day composite for two example weeks from two consecutiv months, March and April 1983. The data are displayed as average over a 5×5 degree area. The map indicates significant changes i the NDVI in the high latitudes over North America, over much o central Europe, and central and northern South America, and sma changes in the NDVI for regions of sparse vegetation such as ove deserts. The map also hints at the problems associated with inter pretation of satellite imagary over polar regions covered by ice an snow among others. While large vegetation changes have occurre in some regions, some of the mapped differences may be due to nois introduced by clouds and aerosols, as well as by changing values o the bidirectional reflectances associated with different viewing an solar geometries. Aspects of these complications are discussed late in Chapter 6.

4.6 Notes and Comments

4.1. The topic of optical properties of condensed matter is a field of study that is too extensive to be covered adequately by a single volume, let alone a single chapter of a book. The aim of this chapter is to provide the reader with a conceptual interpretation of the optical properties that appear in various remote sensing applications. Some of the material given in Sections 4.1 and 4.2 are taken from Feynman et al. (1977, Volumes I and II). More detailed discussions on the topic are found in Bohren and Huffman (1983) and references located therein. A good elementary discussion of local electric field effects is provided in the book of Kittel (1971).

4.2 Basic presentation of the Lorentz and Debye models are given by Born (1965) and von Hippel (1954). One might hesitate to use the simple single oscillator model described in this chapter to represent the optical properties of solids and liquids. Bohren and Huffman (pp. 241–43) provide an impressive "textbook" example of how this one–oscillator model fits the reflection spectrum of α–SiC extremely well. They also show how a multiple oscillator model accurately represents the reflection spectrum of MgO (their Fig. 9.7, p. 246).

4.3. The optical properties of water and ice have been studied for centuries. Warren (1984) provides perhaps the most extensive review of the refractive index data for water extending from the ultraviolet to the microwave. Liebe et al. (1991) describe a model of the optical properties of water at microwave frequencies.

The delay of radio waves propagating in the moist atmosphere is a topic of some importance to microwave remote sensing (e.g. Elgered, 1992). For example, a microwave pulse sent from a satellite and returned to the satellite after being reflected from the ocean surface suffers a delay due to the underburden of water vapor. It is important to deduce this delay in order to map the sea surface with a precision of approximately 1 cm. In this space application, the correction for the effects of water vapor on the refractive index amounts to a delay of several centimeters. Walter (1992b) describes an experimental set up to measure these delays.

Bricaud and Morel (1986) introduce a method for deriving the refractive index based on the inversion of particle scattering measurements. The procedure utilizes the anomalous diffraction formulas that will be introduced in Chapter 5.

4.5. Microwave sensing of surface properties is discussed extensive in the reference text of Ulaby et al. (1986). The reader interest in a more detailed theoretical and observational account of oce and land surface remote sensing, including wave slope effects on m crowave emission, sea–ice remote sensing among many other topic should consult that book. Another text relating to microwave sen ing, primarily of surface properties, is that of Tang et al. (1985). more recent example of a microwave land classification scheme usir a space–borne microwave imager is described in the study of Nea et al., (1990).

There are even more empirical approaches to the estimation surface wind speed (e.g., Goodberlet et al., 1989) and more sophi ticated models of microwave surface emissivity (e.g., Petty, 1990).

The remote sensing of land surface properties is a topic exte sively covered in several texts on remote sensing. For example, Elac (1987) heavily emphasizes surface–property remote sensing as do th texts of Rees (1990) and Sabins (1982).

The application of AVHRR data to land–cover classification an the monitoring of vegetation dynamics was introduced by Tuck (1978, 1979). Spectral measurements of reflected sunlight are als extensively used in geological exploration using spectrometers flow on aircraft. The reflection spectra of geological materials is strongl influenced by crystal lattice structure and composition and the wid variety of geological material complicates the interpretation of thes spectra.

4.7 Problems

4.1. Explain or interpret the following in just one or two sentences
   a. Would you expect sound waves to obey the laws of reflectio or refraction obeyed by light waves?
   b. Why does a diamond sparkle nore than a glass imitatio cut to the same shape?
   c. Can (i) reflection phenomona or (ii) refraction phenomen be used to determine the wavelngth of light?
   d. Observed during daylight hours at 3.7 μm by a sensor o satellite, ice clouds appear darker than an equivalent thick ness water cloud.
   e. Measurements of upwelling 19 GHz polarized microwav radiation incident on a satellite detector discriminates col rain from surface water.

7.5 Principles of Sounding by Emission

An important application of the particular type of radiative transfer discussed in this chapter centers on the inversion of the radiative transfer equation to retrieve vertical distributions of temperature and trace gas concentrations. The general basis of this inversion was outlined in the introductory chapter and much more can be found in the literature cited at the back of this chapter. This section intends only to provide the reader with a broad understanding of the physical basis for temperature sounding.

The basic approach of emission sounding of temperature is to detect the radiation emitted by gases of known distribution, like that of the uniformly mixed gases and specifically by the carbon dioxide molecule at wavelengths centered at 15 μm and by the oxygen molecule at frequencies around 60 GHz.

In discussing how temperature is retrieved from spectral intensity measurements, consider the following two experiments. The first setup has a radiometer at the ground and the second has a radiometer on a satellite that orbits the Earth. It is convenient to introduce

$$\mathcal{T}(t,\tau,\mu) = e^{-(t-\tau)/\mu} \tag{7.29}$$

as the transmittance along the path from the optical depth t to the optical depth τ along the direction defined by μ which we take to be the cosine of the zenith angle of observation. Therefore,

$$\frac{d\mathcal{T}}{dt}(t,\tau,\mu) = -\frac{1}{\mu}e^{-(t-\tau)/\mu} \tag{7.30}$$

and, on substitution into (7.6a), we obtain

$$I(\tau,\mu) = I(\tau^*,\mu)\mathcal{T}(\tau^*,\tau,\mu) + \int_{\tau^*}^{\tau} \mathcal{B}(t)\frac{d\mathcal{T}}{dt}(t,\tau,\mu)dt \tag{7.31}$$

The following notation

$$\mathcal{W}(\tilde{z}_1,\tilde{z}_2) = \frac{d\mathcal{T}}{d\tilde{z}}(\tilde{z}_1,\tilde{z}_2)$$

is used to refer to the quantity known as the *weighting function* for the reasons that become apparent later. In this definition, $\tilde{z}$ is taken to be an arbitrary vertical coordinate system such as altitude z, optical depth τ as in the case of (7.31), pressure p or $\ln p$. Therefore,

the weighting function is defined at some level $\tilde{z}_1$ relative to th measurement level $\tilde{z}_2$. In terms of this general vertical coordinat (7.31) becomes

$$I(\tilde{z},\mu) = I(\tilde{z}^*,\mu)\mathcal{T}(\tilde{z}^*,\tilde{z},\mu) + \int_{\tilde{z}^*}^{\tilde{z}} \mathcal{B}(\tilde{z}')\mathcal{W}(\tilde{z}',\tilde{z},\mu)d\tilde{z}' \tag{7.32}$$

from which the meaning of the weighting function $\mathcal{W}$ emerge Within the context of (7.32), the contribution to the intensity mea sured by a radiometer located at $\tilde{z}$ due to the emission from th layer $\Delta\tilde{z}'$ centered at $\tilde{z}'$ is determined from the local layer blac body emission $\mathcal{B}(\tilde{z}')$ *weighted* by the factor $\mathcal{W}(\tilde{z}',\tilde{z})\Delta\tilde{z}'$. The fun tional form of $\mathcal{W}$ is of fundamental importance to vertical soundin problems and simple models are now described in an attempt t build an understanding of the general properties of $\mathcal{W}$ and how depends on the strength and distribution of absorber.

7.5.1 Weighting Functions for Nadir Sounding

Absorption by molecules in the atmosphere below 50 km is strongl influenced by the collision broadening processes expressed in ter of the Lorentz line shape (refer to Chapter 3),

$$k_\nu = \frac{S\tilde{p}\alpha_{Lo}/\pi}{(\nu-\nu_o)^2 + \alpha_{Lo}^2\tilde{p}^2} \tag{7.33}$$

where α_{Lo} is the line width defined at a pressure $p_o = 1$ atmospher $\tilde{p} = p/p_o$ where p is the pressure in the same unit, S is the lir strength and ν_o is the frequency of the line center. For a gas un formly mixed in the atmosphere with a mass mixing ratio r, it follow that the optical depth of a layer between defined pressure levels p' and p'' is (e.g., Section 3.3c)

$$\tau_\nu = \frac{r}{2p_o g}\int_{p'}^{p''} \frac{Sp\alpha_{Lo}/\pi}{(\nu-\nu_o)^2 + \alpha_{Lo}^2 p^2}dp \tag{7.34}$$

and for absorption in the line wings where $\nu - \nu_o > \alpha_{Lo}p$,

$$\tau_\nu \approx \frac{k_o r}{g}[p'^2 - p''^2] \tag{7.35}$$

where $k_o = S\alpha_{Lo}/\pi(\nu-\nu_o)^2$. For an atmosphere in hydrostat equilibrium, $p = p_o e^{-z/H}$ where H is the atmospheric scale heigh and it follows from (7.35) that

$$t(z) = \tau^* e^{-2z/H} \tag{7.36}$$

where $p' = 0$, and $\tau^* = k_o r p_o / 2g$. Let us define the weighting function relative to the satellite altitude ($z = \infty$) as

$$\mathcal{W}(z, \infty) = \frac{d\mathcal{T}}{dz}(z, \infty) \tag{7.37}$$

then substituting $\exp(-t)$ for $\mathcal{T}(z, \infty)$ and with (7.36) into (7.37), we obtain

$$\mathcal{W}(z, \infty) = \frac{d\mathcal{T}(z, \infty)}{dt}\frac{dt}{dz} = \frac{2\tau^*}{H}\exp\left[-\frac{2z}{H} - \tau^* e^{-2z/H}\right] \tag{7.38}$$

The characteristic relationship between $\mathcal{W}$ and z given by this simple formula is shown in Fig. 7.16a for three different values of τ^*. The shape of the weighting function is governed by two factors: the factor $\exp(-2z/H)$ which decreases with increasing z and the factor $\exp[-\tau^* \exp(-2z/H)]$ which increases as z increases. The first of these factors represents the decrease in absorber gas with changing z and the second factor characterizes the increase in transmission as the path decreases to 0 as z approaches the satellite altitude. These combine to produce a familiar bell-shaped weighting function curve. The width of this curve ultimately characterizes the vertical resolution of the retrieval (refer to Problem 7.5 as an example of this) and the peak of the curve occurs at

$$z_{max} = \frac{H}{2}\ln \tau^*$$

which follows by setting $d\mathcal{W}/dz = 0$. Therefore, measurements at different frequencies characterized by different values of τ^* allow us to sample the emission from different layers in the atmosphere. These layers broadly correspond to the layers that surround the peaks of the corresponding weighting functions. The physical interpretation of the general bell shape of the weighting function curves was discussed in Chapter 3. Near the line center, τ^* is large and the weighting function is more sharply peaked with a maximum higher in the atmosphere. As we move away from the line center toward the wings, τ^* decreases by virtue of the decreasing absorption coefficient. If far enough out from the line center, the maximum of the weighting function actually occurs at the surface (Fig. 7.16a).

The width of lines in the 15 μm CO_2 band varies from about 0.1 to 0.001 cm^{-1} over the range of atmospheric pressures of interest. Most radiometers measure the spectral intensity with a spectral

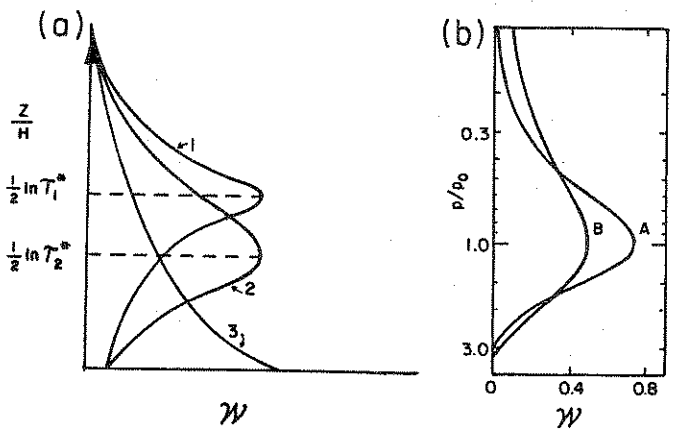

Figure 7.16 (a) The behavior of a monochromatic weighting function $\mathcal{W}$ in the wing of a collision broadened line corresponding to a hydrostatic atmosphere for different value ranges of τ^*, the total optical depth of the atmosphere. Curves labeled as 1: $\tau^* > 1$, 2: $\tau \geq 1$ and 3: $\tau^* \leq 1$. (b) The weighting functions for a monochromatic frequency in the wing of a collision broadened line (A), and for a nonmonochromatic band of frequencies containing strong absorption lines (B) (Houghton et al., 1984).

bandwidth that is significantly broader than the width of individual lines so the radiation actually detected by such an instrument results from the collective emissions by a band of hundreds to thousands of lines. The weighting function for a broad interval containing many overlapping absorption lines can be thought of as a superposition of weighting functions of individual lines each characterized by different values of τ^*. The result is a weighting function that is smeared out over several layers and one that is broader than a weighting function derived for single lines. Figure 7.16b provides an actual example of weighting functions calculated using a special type of transmission model to represent the absorption of a spectral interval that contains many spectral lines.

7.5.2 Weighting Functions for Zenith Sounding

The weighting functions characterizing the emission from the atmosphere as measured by an instrument on the ground looking up are very different from those for nadir viewing instruments. To exam-

ine the characteristic shape of these functions, consider the zenith intensity measured at the ground

$$I(\tau^*) = \int_0^{\tau^*} \mathcal{B}(t) e^{-(\tau^* - t)} dt \tag{7.39}$$

which follows from (7.6b) with $I(0, -\mu) = 0$. The transmittance $\mathcal{T}(\tau^*, t) = \exp[-(\tau^* - t)]$ assuming $\mu = 1$ which becomes

$$\mathcal{T}(z, 0) = \exp[-\tau^* + \tau^* e^{-2z/H}] \tag{7.40}$$

by virtue of (7.36). It simply follows that the weighting function

$$\mathcal{W}(z, 0) = \frac{d\mathcal{T}}{dz} = \frac{2z}{H} e^{-\tau^*} \exp\left[-\frac{2z}{H} + \tau^* e^{-2z/H}\right] \tag{7.41}$$

where the major difference between (7.41) and (7.38) is the change in sign inside the exponential, which leads to $d\mathcal{W}/dz < 0$ and predicts that the shape of the weighting function is always of the type labeled 3 in Fig. 7.16a regardless of the value of τ^*. Two factors also dictate the general shape of these weighting functions. The first of these factors, $\exp(-2z/H)$, characterizes the change in absorber with z and the second factor, $\exp[\tau^* \exp -2z/H]$, is the decrease of transmission as z increases upward away from the instrument. For the distribution of absorbing gas considered, an instrument looking up always receives most of its radiation from layers adjacent to the ground. In the line centers, this radiation originates almost exclusively from layers near the surface whereas radiation is received from higher up in the atmosphere for wavelengths located in the line wings although the maximum emission still occurs near the surface where pressure is greatest and the line is broadest.

7.5.3 Weighting Functions for Limb Sounding

An example of the geometric configuration for limb sounding is given in Fig. 7.17. The intensity measured at the satellite can be expressed as the integral of the emission along a line–of–sight that is defined at the tangent altitude h. We write this equation in the form

$$I(h) = \int_\infty^0 \mathcal{B}(s) \frac{d\mathcal{T}}{ds}(s, 0) ds \tag{7.42}$$

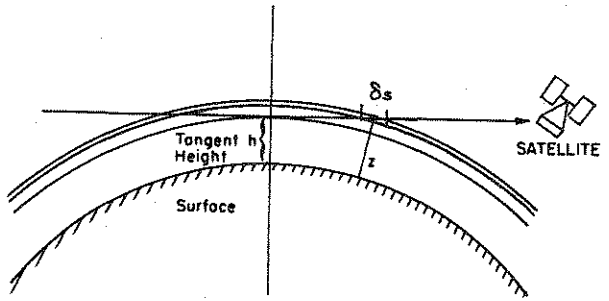

Figure 7.17 Limb viewing geometry. The satellite instrument scans thro the atmosphere along the limb at a tangent height h. Intensity is received fr segments δs of the path at height z.

where $\mathcal{T}(s, 0)$ is the transmission along the path of length s fr the outer levels of the atmosphere at $s = \infty$ through the tang height to the instrument at $s = 0$. As earlier, our analysis consid only the hypothetical case of monochromatic radiation whereas r applications deal with a frequency average over the band pass of t instrument. In reality, an instrument also has a finite field of vi and measures the radiation over some finite vertical layer. In t case of vertical sounding, it is usually assumed that the intensity uniform across the instrument field of view. Although this gen ally does not apply for limb sounding because the intensity typica varies rapidly across the field of view, it is nevertheless assumed he merely to simplify matters.

It is also possible to carry out a simple analysis of the properti of the weighting functions for limb sounders assuming a small fie of view of the instrument and a single frequency response. We u the approach developed earlier for nadir sounding and rewrite (7.4 in the form

$$I(h) = \int_h^\infty \mathcal{B}(z') \frac{d\mathcal{T}}{ds}(z', \infty) \frac{ds}{dz'} dz' \tag{7.4}$$

where the integration is now over altitude z rather than over the ta gent path s. We can relate s to z using simple geometric argumen to obtain the approximation

$$s^2 \approx 2R(z - h)$$

With a vertical weighting function defined as

$$\mathcal{W}(h;z,\infty) = \frac{d\mathcal{T}}{ds}(z,\infty)\sqrt{R/2(z-h)} \quad z > h$$

$$\mathcal{W}(h;z,\infty) = 0 \quad z < h, \tag{7.44}$$

then (7.43) becomes

$$I(h) = \int_h^\infty \mathcal{B}(z')\mathcal{W}(h;z',\infty)dz' \tag{7.45}$$

The square root factor in the definition of $\mathcal{W}$ represents the enhancement of the tangent path relative to a vertical path. Because of this factor, the tangent path defines an absorber amount that is several times larger than that of the vertical path. This enhancement of the absorber path increases the sensitivity of the emission from trace gases such as CO, NO, N_2O, and ClO providing the sensitivity necessary for sounding these gases.

To calculate the weighting functions relevant to limb sounders, the contribution to the measured intensity due to the emission by a layer Δz thick located at z is required. Assuming the geometry of Fig. 7.17, the emission from the layer located about height z follows from (7.43) as

$$\Delta I(z) = \frac{d\bar{\mathcal{T}}}{ds}(z,\infty)\sqrt{R/2(z-h)}[e^{-\tau_1} + e^{-\tau_2}]\mathcal{B}(z)\Delta z \tag{7.46}$$

where

$$\tau_1 = r\int_z^\infty k_m(z')\rho_{air}(z')\sqrt{R/2(z'-h)}dz'$$

and

$$\tau_2 = \tau_1 + 2r\int_h^z k_m(z')\rho_{air}(z')\sqrt{R/2(z'-h)}dz'$$

Here the atmosphere has been divided into two regions; one is the region above the reference level z and nearer to the satellite than the tangent point and the other is that portion of the atmosphere behind the reference level including the path through the layer defined by h and z. τ_1 is the optical path for the first of these paths and τ_2 corresponds to the second and longer path. The factor of two results

and z. Using the hydrostatic assumption, together with an assumed Lozentz line profile,[4]

$$\tau_1 = \frac{\tau^*}{2}\sqrt{\pi HR}[1 - \text{erf}(\sqrt{2(z-h)/H})]\exp(-2h/H), \tag{7.47a}$$

and

$$\tau_2 = \tau_1 + \tau^*\sqrt{\pi HR}\ \text{erf}(\sqrt{2(z-h)/H})\exp(-2h/H), \tag{7.47b}$$

where erf is the error function. The weighting function then follows from (7.45) and (7.46) as

$$\mathcal{W}(h;z,\infty) = \tau^*\sqrt{R/2(z-h)}\exp(-2z/H)[e^{-\tau_1} + e^{-\tau_2}]. \tag{7.48}$$

Figure 7.18a provides examples of this weighting function for different values of τ^*, with the tangent height $h = 12$ km and other parameters as given. For the larger optical depths, the emission arises from broad layers above the tangent height and closer to the sensor and the contribution from the layers near the tangent height is reduced. For $\tau^* = 0.1$, the main contribution comes from the layer immediately above the tangent height. In reality, the observations are obtained by operating in the optically thin region of the stratosphere and by scanning the sensor field of view. This offers a way of obtaining a high vertical resolution in the sounding. Figure 7.17b presents examples of actual weighting functions derived for a relatively wide spectral interval covering much of the 15μm band of carbon dioxide for various values of the tangent height h.

Some distinct advantages of limb sounding by emission are:

- Relatively high vertical resolution. None of the emitted radiation originates below the tangent point. From simple geometric arguments, the atmospheric shell immediately above the tangent height h contains the longest ray path of any layer and since pressure decreases exponentially with height, a large fraction of the outgoing radiation originates from a layer which is typically a few kilometers above the tangent height. As a result of these factors, the weighting functions are spiked.

[4] Note the assumption of a Lorentz line shape, which is used for convenience here, is not strictly appropriate since Doppler broadening mechanisms will also be important at typical stratospheric pressures and at the wavelengths of relevance

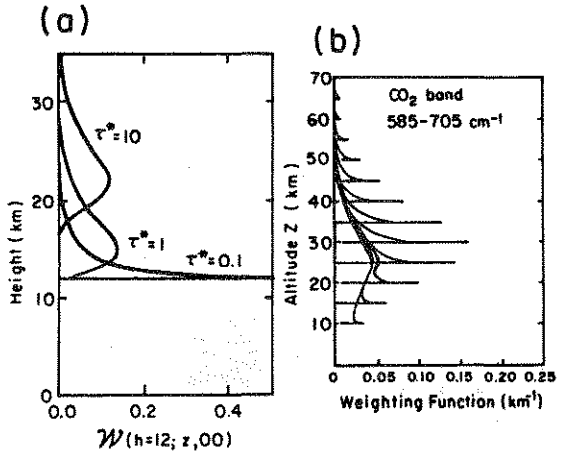

Figure 7.18 (a) The weighting function for limb sounding derived from (7.48) with H=7 km, R=6370 km, and h=12 km for three values of τ^*. (b) A set of weighting functions for a limb sounder based on the ideal case of an instrument with an infinitesimal vertical field of view. The weighting functions are computed for the spectral band 585–705 cm^{-1} which covers most of the 15 μm absorption band of carbon dioxide (after Gille and House, 1971).

- No surface influence on the measured intensities.
- Based on the geometry, considerably more emitting gas (up to about 60 times) exists along grazing paths than along vertical paths. This means that there can be significant contributions by the emission of gases of low concentration than occurs for along vertical paths.

The technique does have certain disadvantages. It is sensitive to the presence of aerosol in the lower stratosphere and generally cannot be reliably used to probe below the tropopause. Limb sounding also requires relatively precise information about the field of view and spacecraft attitudes so that instrument pointing can be accurately determined.

7.5.4 Weighting Functions of an Operational Sounder System

The NOAA TIROS–N Operational Vertical Sounder (TOVS) con-

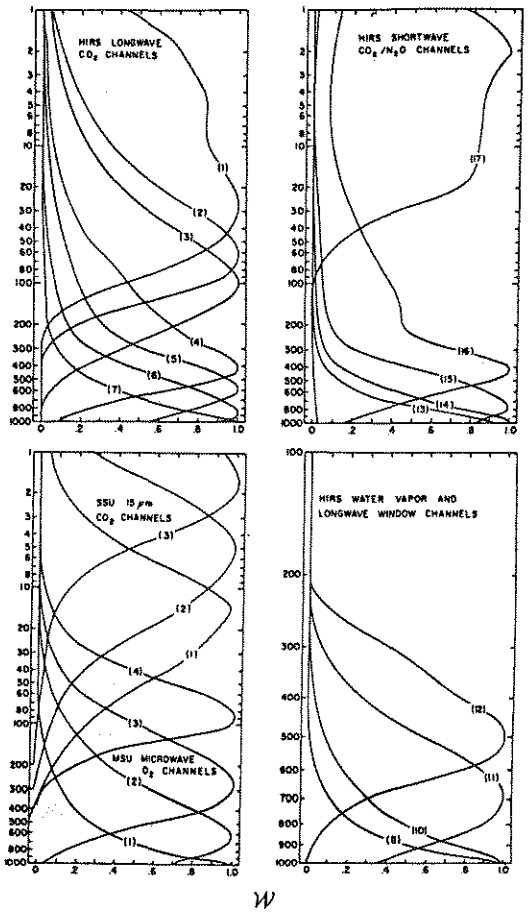

Figure 7.19 Weighting functions for the TOVS sounders (Smith et al., 1979).

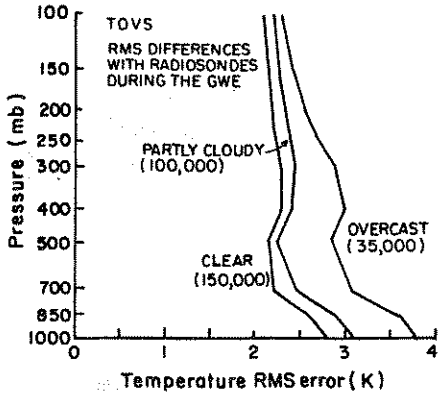

Figure 7.20 Root-mean-square differences between TOVS and radiosonde soundings for an entire year. The collocation and time differences are generally within 200 km and ± 3 hours (Smith, 1991).

High-resolution Infrared Radiation Sounder (HIRS), and the Stratospheric Sounding Unit (SSU). Figure 7.19 presents characteristic weighting functions for each sounder and illustrates the general features predicted by our simple analysis described above.

The actual numerical methods used to retrieve temperature from spectral measurements are not described any further here as these are summarized in some detail by Houghton et al. (1984) and other references noted later. These details are also the subject of the inversion project introduced in Appendix 2. A general assessment of the accuracy of retrieved temperatures is also provided in a number of studies and an example of such an assessment is presented in Fig. 7.20 in the form of the root-mean-square difference between the TIROS-N and radiosonde layer-mean temperatures. This rms difference is around 2-3 K for clear skies but is poorer for partially cloudy conditions and worst for overcast conditions. The reduced accuracy of the overcast sky retrievals is perhaps due to the limited number of tropospheric sounding microwave channels and their poor vertical resolution in the lower troposphere compared to the infrared channels. Although the rms differences of a few degrees shown in Fig. 7.20 seems small, individual differences from radiosondes may be as high as 10 K. These differences typically occur as a result of the coarse vertical resolution of TOVS soundings and the inability to re-

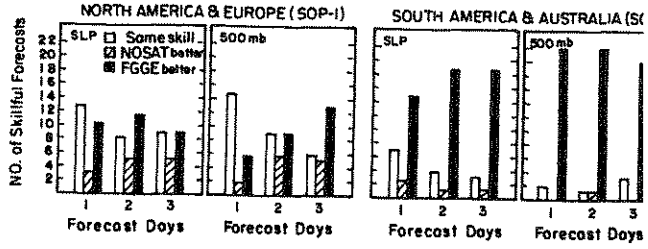

Figure 7.21 Number of cases of positive and negative forecast impa the FGGE observing system with and without satellite data during the p January 5 – March 5, 1979 (Kalnay et al., 1985).

solve sharp temperature gradients. Because of this problem, the difference between TOVS and radiosonde measured temperat tend to be largest near the surface and near the tropopause w vertical temperature gradients are capable of varying significant

Many of the major operational forecast centers of the worl well as a number of numerical modeling research laboratories, l investigated the impact of the TOVS data on numerical forec The general findings from this research are conveniently summar in Fig. 7.21 which is taken from the study of Kalnay et al. (19 This diagram shows the number of times one of two observing tems, the FGGE, which includes satellite data, and the NOS which excludes these data, led to a better forecast when comp to each other[5]. Whereas the results for the northern hemispl are mixed, satellite data proved to be indispensable for analyse low latitudes and in the southern hemisphere. Even in the north hemisphere, satellite data improved the analyses over remote a like the northern Pacific region and helped improve forecasts do stream of that region.

[5] FGGE is the acronym for the First GARP (Global Atmospheric Rese Program) Global Experiment. One of the aims of this experiment was to dev an international observing system for studying the atmosphere and to test t systems during special observing periods throughout an operational year t